JGR Space Physics

RESEARCH ARTICLE
10.1029/2023JA032200

Dispersed Relativistic Electron Precipitation Patterns Between the Ion and Electron Isotropy Boundaries

A. V. Artemyev[1], V. Angelopoulos[1], X.-J. Zhang[1,2], L. Chen[2], and A. Runov[1]

[1]Department of Earth, Planetary, and Space Sciences, University of California, Los Angeles, Los Angeles, CA, USA, [2]Department of Physics, University of Texas at Dallas, Richardson, TX, USA

Key Points:

- We report on observations of patterns of dispersed relativistic electron precipitation in the nightside inner magnetosphere
- These precipitation patterns often show a clear energy versus *L*-shell dispersion
- This new type of precipitation is observed equatorward of the electron isotropy boundary but near or poleward of the ion isotropy boundary

Supporting Information:

Supporting Information may be found in the online version of this article.

Correspondence to:

A. V. Artemyev,
aartemyev@igpp.ucla.edu

Citation:

Artemyev, A. V., Angelopoulos, V., Zhang, X.-J., Chen, L., & Runov, A. (2023). Dispersed relativistic electron precipitation patterns between the ion and electron isotropy boundaries. *Journal of Geophysical Research: Space Physics*, *128*, e2023JA032200. https://doi.org/10.1029/2023JA032200

Received 20 OCT 2023
Accepted 24 NOV 2023

Abstract Relativistic electron precipitation to the Earth's atmosphere is an important loss mechanism of inner magnetosphere electrons, contributing significantly to the dynamics of the radiation belts. Such precipitation may be driven by electron resonant scattering by middle-latitude whistler-mode waves at dawn to noon; by electromagnetic ion cyclotron (EMIC) waves at dusk; or by curvature scattering at the isotropy boundary (at the inner edge of the electron plasma sheet anywhere on the nightside, from dusk to dawn). Using low-altitude ELFIN and near-equatorial THEMIS measurements, we report on a new type of relativistic electron precipitation that shares some properties with the traditional curvature scattering mechanism (occurring on the nightside and often having a clear energy/*L*-shell dispersion). However, it is less common than the typical electron isotropy boundary and it is observed most often during substorms. It is seen equatorward of (and well separated from) the electron isotropy boundary and around or poleward of the ion isotropy boundary (the inner edge of the ion plasma sheet). It may be due to one or more of the following mechanisms: EMIC waves in the presence of a specific radial profile of the cold plasma density; a regional suppression of the magnetic field enhancing curvature scattering locally; and/or electron resonant scattering by kinetic Alfvén waves.

1. Introduction

Relativistic electron losses in the inner magnetosphere can be attributed primarily to three mechanisms that operate in different *MLT* sectors: electron resonant scattering by electromagnetic ion cyclotron (EMIC) waves (e.g., Millan & Thorne, 2007; Shprits et al., 2008), electron scattering by intense middle-latitude whistler-mode waves (Miyoshi et al., 2020; Thorne et al., 2005), and electron curvature scattering by current sheets with small curvature radius (e.g., Artemyev et al., 2013; Sivadas et al., 2019). EMIC waves are usually generated by injected plasma sheet ions along their duskward drift paths that overlap with cold dense plasmaspheric (or plasmaspheric plume) plasma, which favor both the ion-resonant wave excitation and relativistic electron-resonant scattering and subsequent precipitation (Chen et al., 2009, 2011; Jun et al., 2019; Thorne & Kennel, 1971). Alternatively, the day-side magnetosphere compression can produce transversely anisotropic ions responsible for EMIC wave generation in dense plasmaspheric plumes (e.g., Jun et al., 2021). Therefore, EMIC wave-driven electron losses are predominantly near the plasmapause (*L*-shell ∼ 3–5, see O'Brien and Moldwin (2003); Goldstein et al. (2019)) at dusk. Electron curvature scattering requires a thin current sheet around the equatorial plane (Imhof et al., 1977; Sergeev & Tsyganenko, 1982; Sergeev et al., 2012). During substorm growth phase, such current sheets can form at $L \sim 7$–10 (e.g., Sergeev et al., 2011; Artemyev et al., 2016, and references therein), and even inside the geostationary orbit (Angelopoulos, Artemyev, et al., 2020; Sergeev et al., 2008). Therefore, the curvature-driven electron losses are predominantly observed around midnight, at the outer edge of the inner magnetosphere (such a separation of curvature and EMIC wave-driven scatterings is confirmed by observed patterns of ion precipitation, see M. Zhu et al., 2021). Whistler-mode wave scattering of electrons of relativistic energy requires wave propagation to middle latitudes along the magnetic field and the absence of any significant wave Landau damping by suprathermal electrons along the wave propagation (see discussions in Chen et al., 2022; Artemyev et al., 2021). Having low fluxes of such suprathermal electrons, the dayside region (Li et al., 2010; Walsh et al., 2020) is thus the primary *MLT* for relativistic electron losses, due to their resonance with whistler-mode waves at middle latitudes (Elliott et al., 2022, and references therein).

The three aforementioned precipitation mechanisms, namely those driven by EMIC waves, whistler-mode waves, and field line curvature, have distinct features in low-altitude observations. First, EMIC waves which rarely resonate with sub-relativistic electrons (Summers & Thorne, 2003) have electron precipitation spectra usually

exhibiting a clear low energy cutoff. This cutoff can vary even during an event from one hundred to several hundred keV, and is determined by the equatorial background conditions and wave characteristics (see example energy spectra of EMIC wave-driven precipitation patterns in Grach et al., 2022; An et al., 2022; Angelopoulos et al., 2022). Second, precipitation spectra associated with whistler-mode wave relativistic electron scattering are short-lived (for only seconds), resulting in single-spin (or even sub-spin) observations at ELFIN (whose spin-period is ∼2.8 s). They extend to low energies (tens of keV), and are detectable down to the minimum energy measured by ELFIN, 50 keV. Precipitating-to-trapped flux ratios for these waves maximize at the lower energies (see example energy spectra of whistler-driven precipitation patterns in Chen et al., 2022; Zhang et al., 2022). This is contrary to EMIC wave-driven precipitation flux ratios that maximize at the highest detectable energies around 1 MeV or greater. Third, electron field line curvature scattering occurs when the electron gyroradius becomes comparable to the field line curvature radius (see theoretical models in Birmingham, 1984; Delcourt et al., 1994, 1995; Artemyev et al., 2015). As the gyroradius (for a fixed electron energy) increases rapidly and the field line curvature radius decreases rapidly with equatorial distance from Earth, curvature scattering exhibits characteristic energy versus *L*-shell dispersion: lower energy electrons are scattered and thus isotropize in pitch-angle at higher *L*-shells; higher energy electrons do so at lower *L*-shells (Sergeev et al., 2012; Sivadas et al., 2019; Wilkins et al., 2023; Yahnin et al., 1997). For a given energy, the latitude at which isotropy is first observed in a poleward crossing of the ionospheric footpoint of the field lines is called the isotropy boundary for that energy (Imhof et al., 1977; Sergeev et al., 1983). For electrons of energies from tens of keV to a few MeV this boundary maps anywhere from the inner edge of the electron plasma sheet to the outer edge of outer radiation belt (Bloch et al., 2021; Dubyagin et al., 2002; Newell et al., 1998; Sergeev et al., 1993; Wilkins et al., 2023). For ions of similar energies this boundary maps significantly Earthward of the corresponding electron boundary, well within the outer edge of the outer radiation belt. The location and dynamics of the electron and ion isotropy boundaries can also be used to remotely sense the equatorial current sheet configuration (Dubyagin et al., 2021; Sergeev et al., 2018), because the field line curvature as a function of radial distance can be deduced from observations and compared with model predictions. In this study we report on a new type of relativistic electron precipitation, which shares some properties with all three aforementioned mechanisms, but cannot be attributed to any of these (classical) mechanisms. Its origin requires further investigation and can be used to advance our understanding of theoretical models of electron losses.

Using precipitating and locally trapped electron measurements from the two identical ELFIN CubeSats, on a low-altitude, polar orbit (Angelopoulos, Tsai, et al., 2020), we found nightside electron precipitation patterns exhibiting strong losses of relativistic electrons over a broad energy range. The precipitating-to-trapped flux ratio spectra exhibit energy versus *L*-shell dispersion typical of curvature scattering, but observed well-earthward from (equatorward of) the electron isotropy boundary that is also readily recognizable in the same satellite pass. We show examples of such events, which map magnetically to the outer radiation belt, and discuss possible mechanisms responsible for them. Specifically: In Section 2 we introduce electron and ion measurements by ELFIN, and compare them with equatorial spectra measured by the THEMIS (Angelopoulos, 2008) and MMS (Burch et al., 2016) missions. Toward that end, we use observations of the isotropy boundary near the inner edge of the plasma sheet, for which such a quantitative flux comparison is possible, thanks to the mapping knowledge and the flux pitch-angle isotropy during this phenomenon (see, e.g., Artemyev et al., 2022). In Section 3, we show five observations of the new electron precipitation pattern at ELFIN. All are from 2022, when ELFIN also acquired ion measurements while magnetically conjugate to THEMIS at the equator. ELFIN ion measurements allow us to localize the new dispersed electron precipitation patterns relative to the classical ion isotropy boundary, whereas THEMIS measurements place the ELFIN observations in the context of substorm dynamics. In addition to these five events, we found 12 events but without simultaneous ELFIN ion measurements or concurrent equatorial measurements by THEMIS or MMS; these have been included in Supporting Information S1 for completeness. In Section 4, we discuss three possible mechanisms for the observed electron dispersed scattering earthward of the electron isotropy boundary. Section 5 presents our conclusions.

2. Instruments and Data Sets

We use ELFIN measurements between June and September 2022, when ELFIN's orbit was close to the noon-midnight meridian and its nightside observations map to the magnetotail. During this interval ELFIN's energetic particle detectors (EPDe and EPDi, for electrons and ions respectively) collected electron and ion spectra in the 50–6,000 keV energy range (binned in 16 logarithmically distributed energy channels) and [0, 180°]

pitch-angle range (8 angular channels) once per half a spin period. We use ion and electron energy spectra averaged over two pitch-angle ranges: precipitating fluxes, those within the bounce loss-cone, j_{prec}; and locally trapped fluxes, those outside of the bounce loss-cone, j_{trap} (Angelopoulos et al., 2022; Angelopoulos, Tsai, et al., 2020). To only include data with reliable j_{prec} and j_{trap}, we require the minimum number of counts at each energy channel to be larger than 5/spin. Through the text, we mostly analyze j_{prec}/j_{trap} ratio as a measure of the precipitation intensity, whereas spectra of j_{trap} and j_{prec} can be found in SI. During this period, ELFIN crossings of the plasma sheet and the inner magnetosphere on the nightside can be in conjunction with the MMS (Burch et al., 2016) and the inner THEMIS satellites (Angelopoulos, 2008), since the apogees of both missions were at the nightside then. Figures 1 and 2 show two examples of such observations, when the ELFIN orbit tracks mapped within ±2 hr of the MMS and THEMIS MLTs. We use 30–700 keV electron measurements from the THEMIS Solid State Telescope (SST; Angelopoulos et al., 2008), 25–650 keV electron measurements from the MMS Fly's Eye Energetic Particle Spectrometer (FEEPS; Blake et al., 2016), and 20–500 keV ion measurements from the MMS Energetic Ion Spectrometer (EIS; Mauk et al., 2016). To trace local geomagnetic conditions in the magnetotail and to estimate MMS and THEMIS locations relative to the equator, we use magnetic field measurements by the fluxgate magnetometers onboard MMS (Russell et al., 2016) and THEMIS (Auster et al., 2008).

Figures 1a–1d show 2.5 hr of THEMIS and MMS observations in the near-Earth plasma sheet on 2022-07-18. Prior to 09:50 UT the magnetic field component B_x shows clear signatures of thin current sheet formation ($|B_x|$ increases at the off-equatorial MMS and THEMIS D satellites). Subsequently, a strong dipolarization occurred ($|B_x|$ decreases and fluctuates) and was accompanied by a flux enhancement at THEMIS and MMS, corresponding to a substorm onset evident in the AE index (not shown), which increased from 100 to 600 nT in 30 min. After 10:00 UT, THEMIS and MMS observed a plasma sheet filled by energetic ions and electrons, where some of the energetic flux variations are due to the relative motion of the equatorial plane from the satellite (B_x variations) and some due to episodic flux enhancements related to substorm intensifications. We next compare THEMIS E electron flux measurements (Panel (b)) and MMS electron and ion flux measurements (Panels (c,d)) with those at ELFIN.

Around 11:30-11:33 UT, ELFIN A crossed the plasma sheet at low altitude. To compare with MMS and THEMIS, we use j_{trap} fluxes at ELFIN when it was projected to the plasma sheet, where $j_{prec}/j_{trap} \sim 1$ (energetic particle distributions are isotropic) due to strong curvature scattering (see details in Artemyev et al., 2022). Figures 1e2 and 1f2 show electron and ion j_{trap} energy-time spectrograms, respectively, along the ELFIN orbit. The panels right above them, Figures 1e1 and 1f1 show the precipitating-to-trapped flux ratios, j_{prec}/j_{trap}, for those two species, respectively. The electron plasma sheet starts on ELFIN at ∼11:32:05 UT because during its poleward motion the j_{trap} electron spectra (in Figure 1e2) change from having significant fluxes at >300 keV (as expected in the outer radiation belt) to negligible fluxes above that energy (as expected in the plasma sheet). Consistent with this interpretation, the precipitation flux ratio (in Figure 1e1) changes from being <1 at most energies of significant flux, signifying moderate scattering (as expected for scattering by waves in the outer radiation belt) to ≈1, signifying strong scattering (as expected for curvature scattering in the plasma sheet). In the region between 11:31:42UT and 11:32:00UT there is a clear signature of dispersion in the minimum energy of isotropization (precipitation ratio reaching ≈1) versus time (in this satellite pass, latitude increases with time). This is the same as saying that the latitude of isotropy increases with decreasing energy, which is the definition of the isotropy boundary (see Wilkins et al., 2023, and references therein). This interval is therefore the classical electron isotropy boundary for electrons of 50 keV to a few MeV, located between the outer radiation belt and the inner edge of the plasma sheet (straddling both). Using a similar methodology, the ion plasma sheet (defined as the latitude above which trapped fluxes of >300 keV ions become negligible in Figure 1f2) starts at (is poleward of) ∼11:31:35 UT, whereas the ion isotropy boundary is evident as the energy-time dispersed ion isotropization (precipitation ratio reaching ≈1 in Figure 1f1) at ∼11:31:20–∼11:31:30UT. This maps closer to Earth (earlier in time by 20–30 s depending on energy, thus at lower latitude) relative to the electron isotropy boundary of the same energy. This is expected, since ions have larger gyroradii than electrons of the same energy, allowing the ion isotropy boundary to reside closer to Earth (see examples of relative locations of the ion and electron isotropy boundaries in Yahnin et al., 1997; Sergeev et al., 2012, 2018).

Figure 1g shows a comparison of ELFIN electron j_{trap} (collected within $j_{prec}/j_{trap} \sim 1$ region) and near-equatorial THEMIS and MMS electron flux measurements. There is a sharp gradient of j_{trap} across the isotropy boundary: at 11:32:00 UT, ELFIN fluxes (ELF, red solid line) are similar to THEMIS-E (Th-E, black lines, solid and dotted, taken during and well-after an injection that started at 11:22UT). Only 20 s later, by 11:32:20 UT, ELFIN is already projected further downtail in the plasma sheet. At that time ELFIN's j_{trap} spectrum (ELF, red dashed

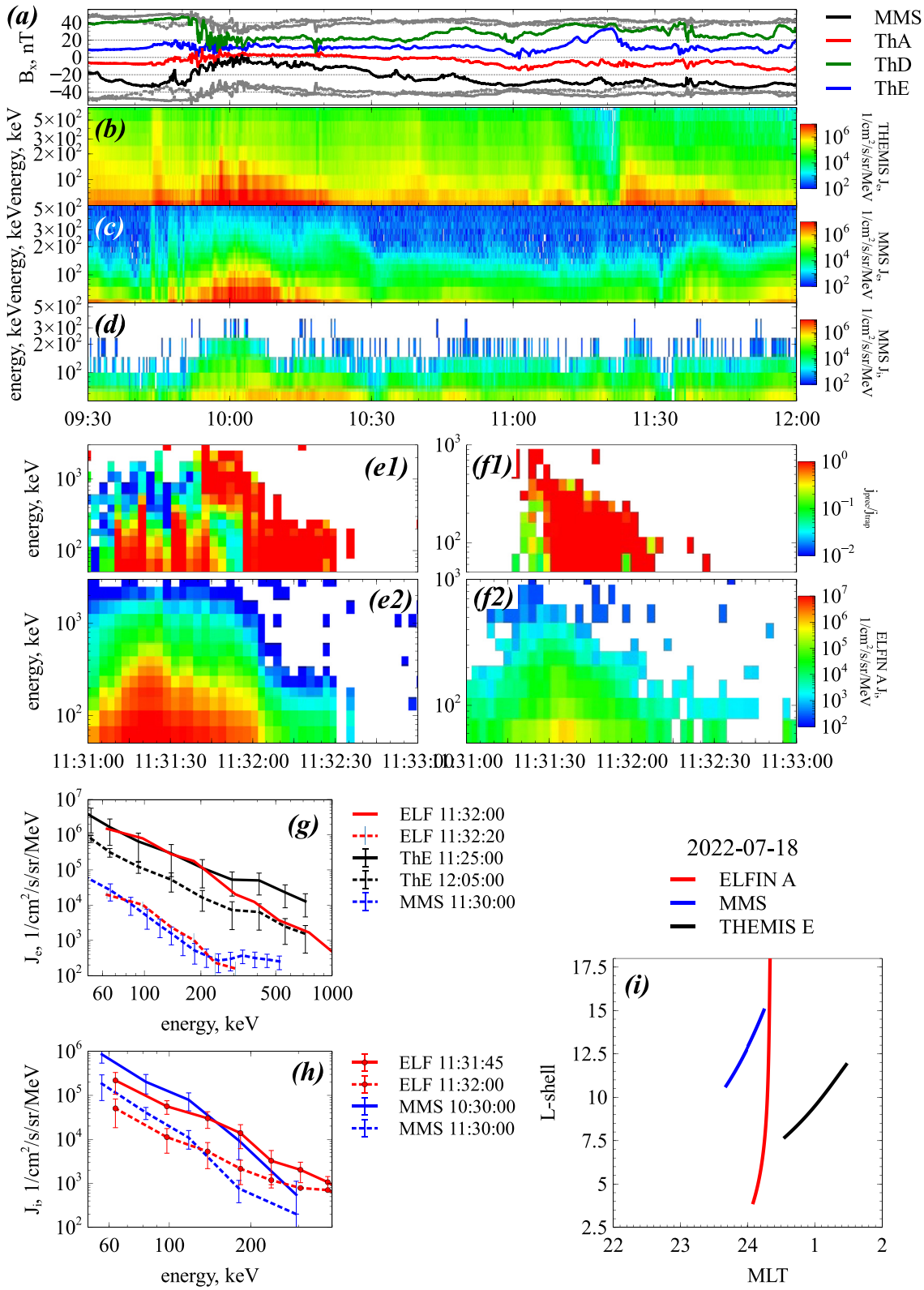

Figure 1. THEMIS E, MMS, and ELFIN A measurements during an example, conjunction event on 2022-07-18 (see Panel (i) for spacecraft orbits projected to the equatorial plane with (Tsyganenko, 1989) model): B_x measurements by three THEMIS spacecraft and MMS #1 spacecraft and $\pm B_{lobe}$ (solid and dashed gray curves for THEMIS D and MMS) (a); THEMIS E SST electron spectrogram (b); MMS FEEPS electron spectrogram (c) and EIS ion spectrogram (d); ELFIN A electron (e1,2) and ion (f1,2) flux ratio j_{prec}/j_{trap} and j_{trap} spectra; comparison of THEMIS, MMS, and ELFIN electron (g) and ion (h) spectra. In Panels (g) and (h), ELFIN spectra are averaged over 6 s intervals, whereas MMS and THEMIS spectra are averaged over 2 min intervals.

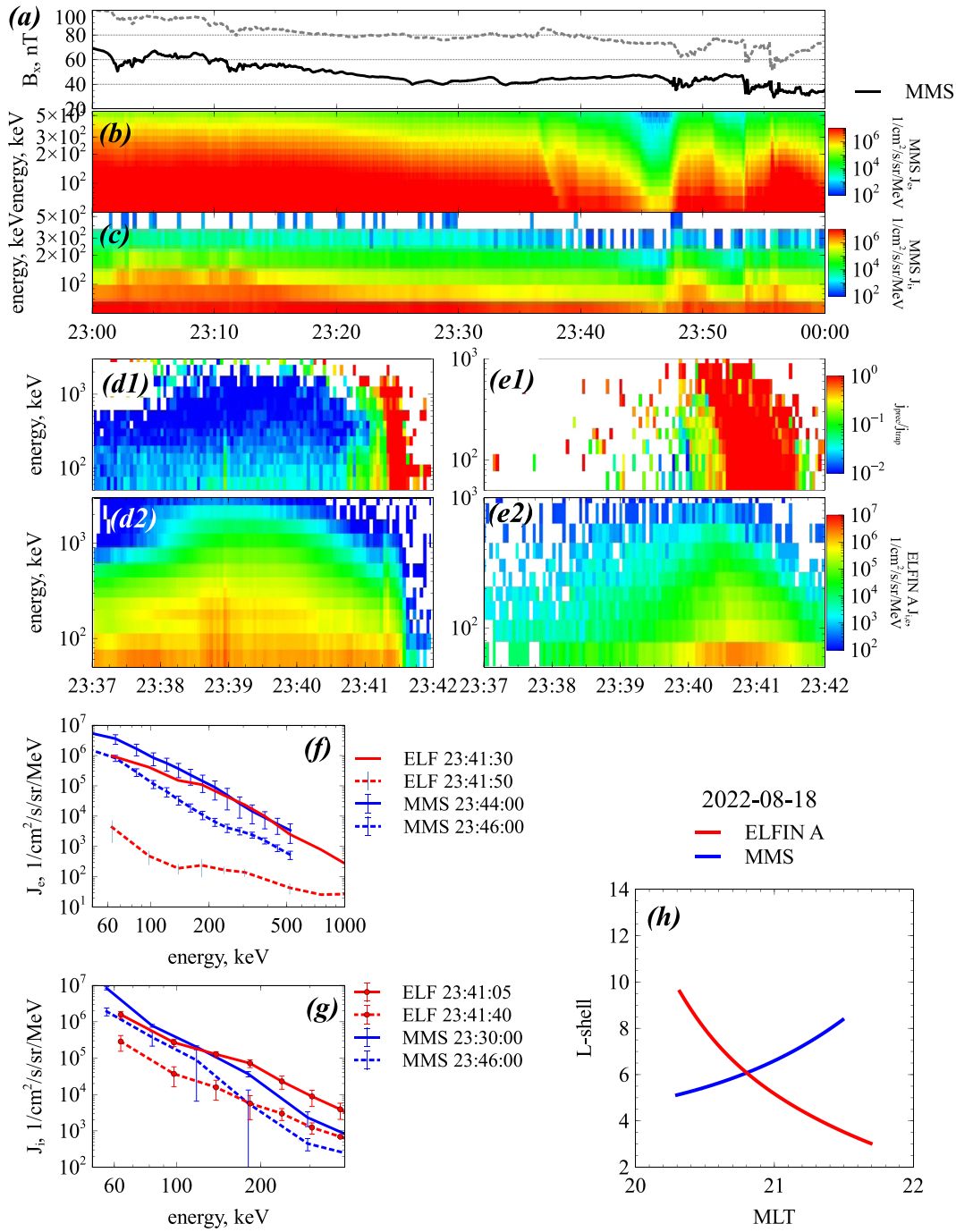

Figure 2. MMS and ELFIN A measurements during another example, conjunction event on 2022-08-18 (see panel (h) for spacecraft orbits projected to the equatorial plane with (Tsyganenko, 1989) model): B_x measurements by MMS #1 spacecraft and B_{lobe} (gray dashed curve) (a); MMS FEEPS electron (b) and EIS ion (c) spectra; ELFIN A electron (d1,2) and ion (e1,2) flux ratio j_{prec}/j_{trap} and j_{trap} spectra; comparison of MMS and ELFIN electron (f) and ion (g) spectra. In Panels (g) and (h), ELFIN spectra are averaged over 6 s intervals, whereas MMS spectra are averaged over 2 min intervals.

line) matches the MMS spectrum (MMS, blue dashed line) taken at approximately the same time. (Note that MMS and THEMIS are separated by ~5R_E, with their equatorial projections having an even larger separation as suggested by the (Tsyganenko, 1989) model.) Comparison of B_x and B_{lobe} (evaluated from the vertical pressure balance, see, e.g., Runov et al., 2006) confirms that MMS is much farther from the equator (its $|B_x/B_{lobe}|$ is larger than THEMIS E).

Given the good agreement between MMS and ELFIN electron spectra, we next compare their ion measurements in Figure 1h. The ion spectrogram of j_{trap} also shows a gradient in the latitudinal (equivalent to a projection in the radial) direction, but this gradient is smoother than the electron one in Figure 1g. The ELFIN ion spectra corresponding to the inner edge of the ion plasma sheet (at 11:31:45 UT) and further tailward (at 11:32:00 UT) are quite similar to the MMS measurements between 10:30 UT and 11:30 UT, when MMS gradually moved away from the equatorial plane ($|B_x|$ increases) and thus captured ion spectra progressively from the more distant magnetotail.

Figure 2 shows an event similar to the one of Figure 1: ELFIN observations of the nightside plasma sheet from a poleward trajectory at the ionosphere in a similar MLT sector as (within ±2 hr of) the near-equatorial MMS spacecraft (see equatorial projections of all spacecraft in Panel (i)). MMS measurements are from the near-Earth plasma sheet ($L \in [5, 9]$); thus MMS ion and electron fluxes (collected after 23:30 UT, when MMS moved out of the inner magnetosphere; see Panels (b,c)) can be compared to ELFIN measurements. ELFIN electron and ion trapped flux measurements falling close to noise level at 300 keV indicate the plasma sheet proper: the electron plasma sheet starts in time from (extends poleward of) 23:41:30 UT (Panels (d1, d2)) and the ion plasma sheet starts from ∼23:41:20 UT (Panels (e1, e2)). These are poleward of ELFIN's crossing of the electron and ion isotropy boundaries (see also Wilkins et al., 2023), which are evident in the dispersion with latitude of the minimum energy where precipitation ratios become ∼1 for electrons and ions, at 23:41:00 - 23:41:20UT for electrons and 23:40:00 - 23:40:30UT for ions respectively, the actual time depending on energy. The comparison of ELFIN electron flux spectra with MMS spectra in Panel (f) confirms that MMS flux measurements at 23:46:00 from the plasma sheet are quite close to ELFIN's near-Earth plasma sheet measurements. Due to stretching of the magnetotail magnetic field lines, the entire plasma sheet projection to low-altitudes shrinks to just a couple of degrees in latitude (see details and examples in Artemyev et al., 2022). At 23:41:50 UT, just 30 s poleward of the electron isotropy boundary of 50 keV electrons and a mere 20 s poleward of the inner edge of the electron plasma sheet (Panel (d)) the electron fluxes on ELFIN are drastically reduced even further (see Panel (b)) becoming much lower than the minimum fluxes measured by MMS at 23:46:00 UT (when MMS is projected downtail; see flux decrease in Panel (b)). Using intervals of a good relation between MMS and ELFIN electron fluxes, we compare MMS and ELFIN ion flux measurements. Panel (g) shows that ion flux measurements from ELFIN (within the $j_{prec}/j_{trap} \sim 1$ region; not shown) are quite close to MMS equatorial flux measurements.

In summary, Figures 1 and 2 demonstrate that ion and electron fluxes measured during ELFIN's traversals of the plasma sheet are quite close to near-equatorial MMS and THEMIS measurements, and thus these two data sets can be analyzed together to unravel mechanisms for electron precipitation. We next focus on a specific pattern of the electron precipitation: energy versus L-shell dispersed relativistic electron precipitation observed earthward of the inner edge of the electron plasma sheet and of the classical electron isotropy boundary. Table 1 lists 17 such events collected in 2020–2022 when ELFIN was projected to the magnetotail. The first five events from this list have simultaneous ion measurements at ELFIN and equatorial measurements from THEMIS, and are thus analyzed in detail in Section 3, whereas the other 12 events only have ELFIN electron measurements but no simultaneous equatorial measurements, and are left in Supporting Information S1.

3. Typical Events

Figure 3 shows observations during the first event from Table 1: ELFIN observations are in the main phase of a moderate storm with $SymH \approx -50$ nT and $AE > 500$ nT for more than 12 hr (Panel (a)). THEMIS observations within ±1 hr of ELFIN's pass under consideration show at least two moderate dipolarizations on THEMIS-D (Th-D), one at 11:35UT and another at 11:59UT (Panels (g,h)). Locally trapped electron and ion fluxes at ELFIN (Panels (b-e)) show that the plasma sheet is extended in latitude and filled with energetic particles, likely the result of injections associated with the aforementioned dipolarization at THEMIS-D. The electron isotropy boundary for 1 MeV electrons is crossed at around 11:52:30 UT, and that for 50 keV electrons is crossed at around 11:53:30 UT. The energy of transition to near-isotropy as exhibited by the j_{prec}/j_{trap} flux ratio ($j_{prec}/j_{trap} > 0.5$) is dispersed in time, with higher energies isotropized at earlier times, corresponding to lower L-shells. However, the progression in the isotropy boundary is not continuous, likely due to the dynamic conditions during the storm. A gap in the monotonic progression in isotropy latitude (increase) versus isotropy minimum energy (decrease) is seen at 11:52:45UT. A gap in the isotropic nature of the fluxes at all energies expected poleward of the isotropy boundary of 50 keV electrons (11:53:30 UT) is seen between 11:53:35UT and 11:54:30UT where the flux ratio drops temporarily below 0.2. We attribute both deviations from expected behavior to dipolarizations and associated

Table 1
List of Events When ELFIN Observed Relativistic Electron Precipitation With Energy/L Dispersion

#	Date	Time	Figures	*L*-shell	*MLT*
1	2022-07-19	11:50:30–11:56:00	Figure 3	~6	~0
2	2022-08-11	09:37:00–09:40:30	Figure 4	~12	~23.5
3	2022-08-19	05:41:00–05:46:30	Figure 5	~7	~23
4	2022-08-19	06:05:00–06:11:00	Figure 6	~7	~23
5	2022-08-07	21:55:30–21:59:00	Figure 7	~4.5	~21.5
6	2020-09-27	18:29:00–18:31:30	Figure S1 in Supporting Information S1	~6.5	~0
7	2020-09-27	20:03:30–20:07:00	Figure S2 in Supporting Information S1	~6	~0.5
8	2020-10-01	20:41:30–20:44:30	Figure S3 in Supporting Information S1	~12	~23
9	2020-10-03	21:01:30–21:03:00	Figure S4 in Supporting Information S1	~15	~22.5
10	2020-10-25	18:01:00–18:03:00	Figure S5 in Supporting Information S1	~10	~23
11	2021-09-17	19:05:00–19:07:00	Figure S6 in Supporting Information S1	~4.5	~0
12	2021-10-12	04:00:00–04:04:00	Figure S7 in Supporting Information S1	~3.5	~22
13	2021-11-16	04:09:00–04:12:00	Figure S8 in Supporting Information S1	~6	~22.5
14	2021-12-01	14:45:00–14:47:00	Figure S9 in Supporting Information S1	~5	~20.5
15	2021-12-10	14:43:00–14:47:00	Figure S10 in Supporting Information S1	~4.5	~20.5
16	2022-06-20	11:45:00–11:48:00	Figure S11 in Supporting Information S1	~12	~1.5
17	2022-06-25	18:36:30–18:39:00	Figure S12 in Supporting Information S1	~5	~0.25

Note. Last two columns show the location of dispersed precipitation events. ELFIN *L*-shell evaluated with (Tsyganenko, 1989) model is not accurate during substorm dynamics (see Artemyev et al., 2022).

injections, like the transient dipolarizations seen at THEMIS D at ~11:35 UT and ~11:59 UT (see Y. Shen et al., 2023, for detailed analysis of such type of transient events). In such instances, the mapping changes abruptly (with the sudden appearance of dipolarized flux bundles in the inner magnetosphere and at the near-Earth plasma sheet) causing a fixed latitude in the ionosphere previously projected to the mid-tail plasma sheet to rapidly map to lower *L*-shells, well within the inner magnetosphere (Chu et al., 2015; Nikolaev et al., 2015). Similarly, the inner edge of the electron plasma sheet (where >300 keV electron fluxes fall below noise level in a poleward satellite track) is also dynamic: it first appears at 11:54:15UT but as the fluxes increase again, it reappears later, near the end of the pass, at 11:55:55UT. Again, we attribute this to the variability in magnetic mapping, due to plasma sheet dynamics at the time.

The inner edge of the ion plasma sheet (where the >300 keV ion fluxes fall below noise level) is first encountered at 11:54:15 UT, and then again at 11:55:30 UT. The ion isotropy boundary, is very sharp, hence poorly resolved, at 11:52:00–11:52:12 UT, and its detection is also complicated by plasma sheet dynamics affecting the magnetic mapping. Despite the dynamics, it is clear that between 11:52:12–11:53:00 UT, ELFIN is at the outer edge of the outer radiation belt (since relativistic electrons <500 keV are not field-line scattered to isotropy and their trapped fluxes are high), but still at or poleward (tailward) of the ion isotropy boundary that lies equatorward of 11:52:12 UT. Within this region, ELFIN also observed occasionally sub-relativistic (<300 keV) electron precipitation bursts (evident at 11:52:30 UT in Panel (c)), likely due to equatorial electron scattering by whistler-mode waves (see detailed analysis of such events in Tsai et al., 2022).

Just equatorward of the electron isotropy boundary of 2 MeV electrons and of the concurrent whistler-mode wave precipitation, that is, inside the outer radiation belt, ELFIN observed precipitation of >500 keV electrons with $j_{prec}/j_{trap} \sim 0.2$–$0.9$ at 11:52:05 UT (Panel c). This precipitation occurred concurrently with the ion isotropy boundary (Panel (e)). It cannot be attributed to the classical electron isotropy boundary, because the location of curvature scattering for electrons must be poleward of that for ions of the same energy, due to the vastly different gyroradii of electrons and ions in the same equatorial magnetic field.

Figure 4 shows another example similar to the one described above, which occurred during the growth phase of a strong substorm (see Panel (a)) instead of a storm. The plasma sheet configuration exhibits the formation

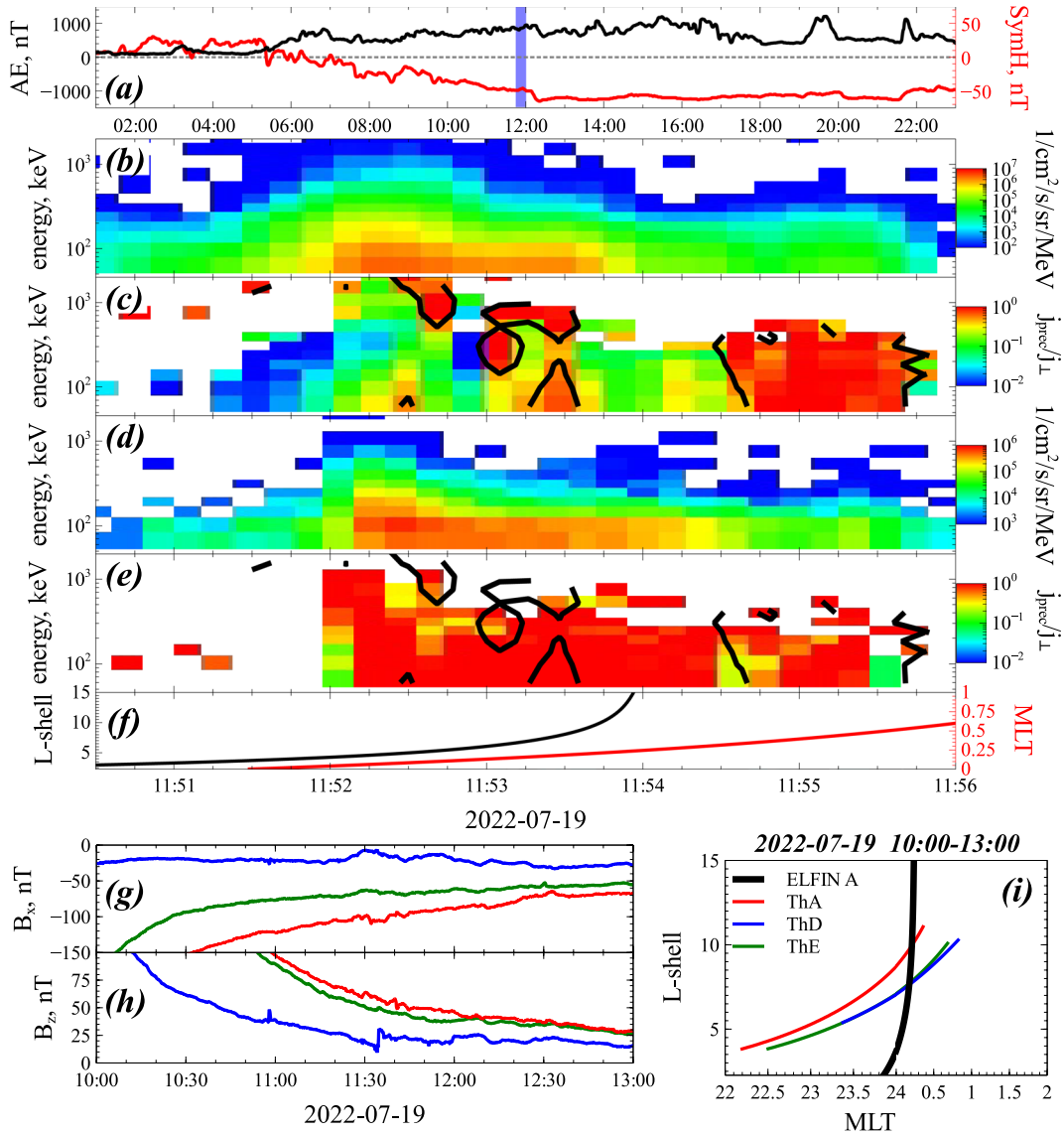

Figure 3. Overview of measurements during the event on 2022-07-19: (a) *AE* and *SymH* indices during the day (ELFIN event time-period denoted by blue, vertical bar); (b) and (d): locally trapped electron and ion fluxes, respectively; (c) and (e): precipitating-to-trapped flux ratio j_{prec}/j_{trap} for electrons and ions, respectively (black contours in both panels mark where electron $j_{prec}/j_{trap} = 0.9$); (f) ELFIN *L*-shell and *MLT* from T89 (Tsyganenko, 1989) model; (g) and (h): B_x and B_z, respectively, from three THEMIS spacecraft during a three-hour interval encompassing the ELFIN event; (i) ELFIN and THEMIS orbits projected to the (*MLT*, *L*) plane for the same three-hour interval.

of a thin current sheet followed by dipolarization at 10:30 UT (see B_x and B_z evolution in Panels (g, h) and a detailed description of such events in, for example, Artemyev et al. (2016)). During the current sheet thinning (substrom growth phase), the electron plasma sheet projection at low altitudes almost disappears, shrinking to a couple of degrees in latitude (or ∼30 s in duration at ELFIN) (see Artemyev et al., 2022). Indeed, Panels (b, c) show only short glimpses of the plasma sheet (several ELFIN spins with <200 keV fluxes after 09:39:45 UT), whereas the electron isotropy boundary (seen for 50 to 300 keV electrons) is encountered over a very short latitude range (unresolved by ELFIN's spin resolution) $j_{prec}/j_{trap} \sim 1$ within a single ELFIN spin at 09:39:30 UT. Equatorward from that location ELFIN detected two classically dispersed precipitation patterns of the minimum energy where the ratio was ∼1 at energies 300 keV to 3 MeV (09:38:30–09:38:45 UT and 09:39:15–09:39:30 UT), as expected for the isotropy boundary at those energies (a decrease in that minimum energy with increasing latitude). However, the reverse pattern was also seen: the minimum energy where $j_{prec}/j_{trap} \sim 1$ increased with

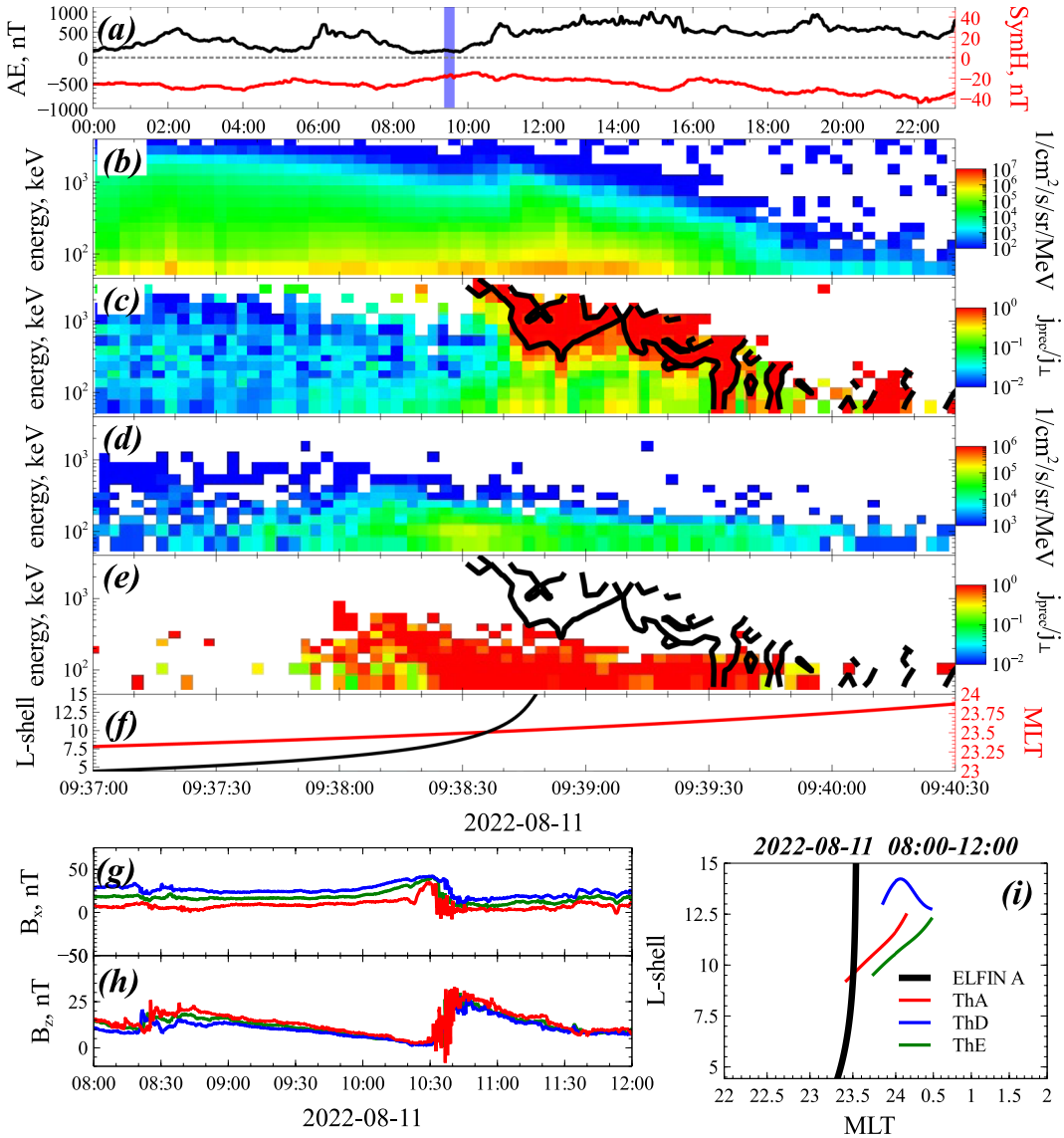

Figure 4. Overview of measurements during the event on 2022-08-11: (a) *AE* and *SymH* indices within a day, the ELFIN orbit is denoted by a blue, vertical bar; (b, d) locally trapped electron and ion fluxes; (c, e) electron and ion precipitating-to-trapped flux ratio j_{prec}/j_{trap}, black contours in both panels mark where electron $j_{prec}/j_{trap} = 0.9$; (f) ELFIN *L*-shell and *MLT* from T89 (Tsyganenko, 1989) model; (g, h) B_x and B_z measurements from three THEMIS spacecraft during a three-hour interval; (i) ELFIN and THEMIS orbits projected to the (*MLT*, *L*) plane.

latitude between 09:38:25 UT and 09:39:10 UT. Both patterns are well within the outer radiation belt, featuring trapped relativistic electrons (Panel (b)), but poleward from the ion isotropy boundary of >50 keV ions, which was seen equatorward of 09:38:20 UT. These two new forward precipitation patterns plus the reverse one between them collectively lasted about 1 minute, which is much longer than a typical electron isotropy boundary, especially during the substrom growth phase (see Artemyev et al., 2022; Wilkins et al., 2023).

To demonstrate the stability of energy/*L*-shell dispersed patterns, we examine two successive orbits from ELFIN A and B separated by 25 min Figures 5 and 6 show the data for those orbit, captured at the nightside during quiet geomagnetic conditions: small *AE* and with no signatures of current sheet dynamics/injections at the THEMIS satellites (see Panels (a, g, h)). Both ELFIN spacecraft observed a prolonged electron plasma sheet (after 05:44:40 UT and 06:08:40 UT with $j_{prec}/j_{trap} \sim 1$ at <300 keV and j_{trap} near noise level at >300 keV). The electron isotropy boundary for 50–200 keV electrons is observed in Figure 5c around 05:44:35 UT, and in Figure 6c around 06:08:15 UT. These boundaries can be distinguished by reductions in the intensity of sub-relativistic electron

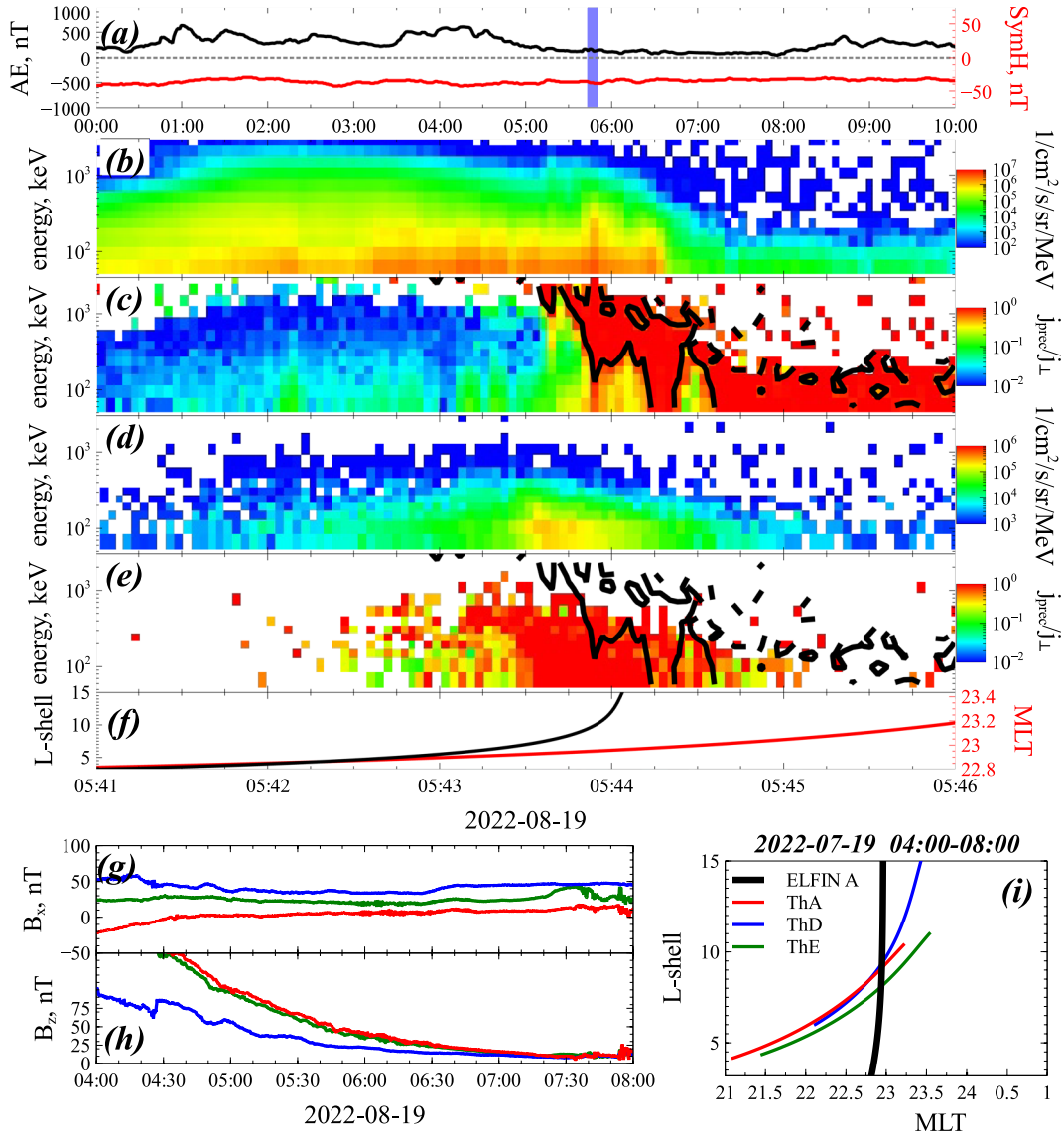

Figure 5. Overview of measurements during the event on 2022-08-19: (a) *AE* and *SymH* indices within a day, the ELFIN orbit is denoted by a blue, vertical bar; (b, d) locally trapped electron and ion fluxes; (c, e) electron and ion precipitating-to-trapped flux ratio j_{prec}/j_{trap}, black contours in both panels mark where electron $j_{prec}/j_{trap} = 0.9$; (f) ELFIN *L*-shell and *MLT* from T89 (Tsyganenko, 1989) model; (g, h) B_x and B_z measurements from three THEMIS spacecraft during a three-hour interval; (i) ELFIN and THEMIS orbits projected to the (*MLT*, *L*) plane.

precipitation equatorward of them. Further equatorward of those reductions, both ELFIN satellites captured again dispersed signatures in the minimum energy of intense precipitation ratio (∼1) versus latitude: both forward (similar to a classical isotropy boundary) at energies extending up to several MeV and reverse at energies 50–400 keV. The totality of those dispersed signatures lasted longer in Figure 5c and shorter in Figure 6c. These patterns are well within the outer radiation belt, as relativistic trapped electron fluxes are abundant at those times, but poleward of the isotropy boundaries of 50–400 keV ions that are at 05:43:15 - 05:43:25 UT and 06:07:10 - 06:07:35 UT, respectively. Consistently in both events, the new type of dispersed electron precipitation patterns extend over a wide energy range, from 50 keV to multi-MeV.

Figure 7 shows ELFIN nightside observations during a substorm expansion phase (relative to the *AE* peak in Panel (a)), characterized by strong perturbations of the equatorial magnetic field via multiple dipolarizations and injections (see Panels (g, h)). ELFIN crossed the plasma sheet right during current sheet thinning between two small-scale dipolarizations ($|B_x|$ was increasing and $|B_z|$ was decreasing at all THEMIS spacecraft at the time

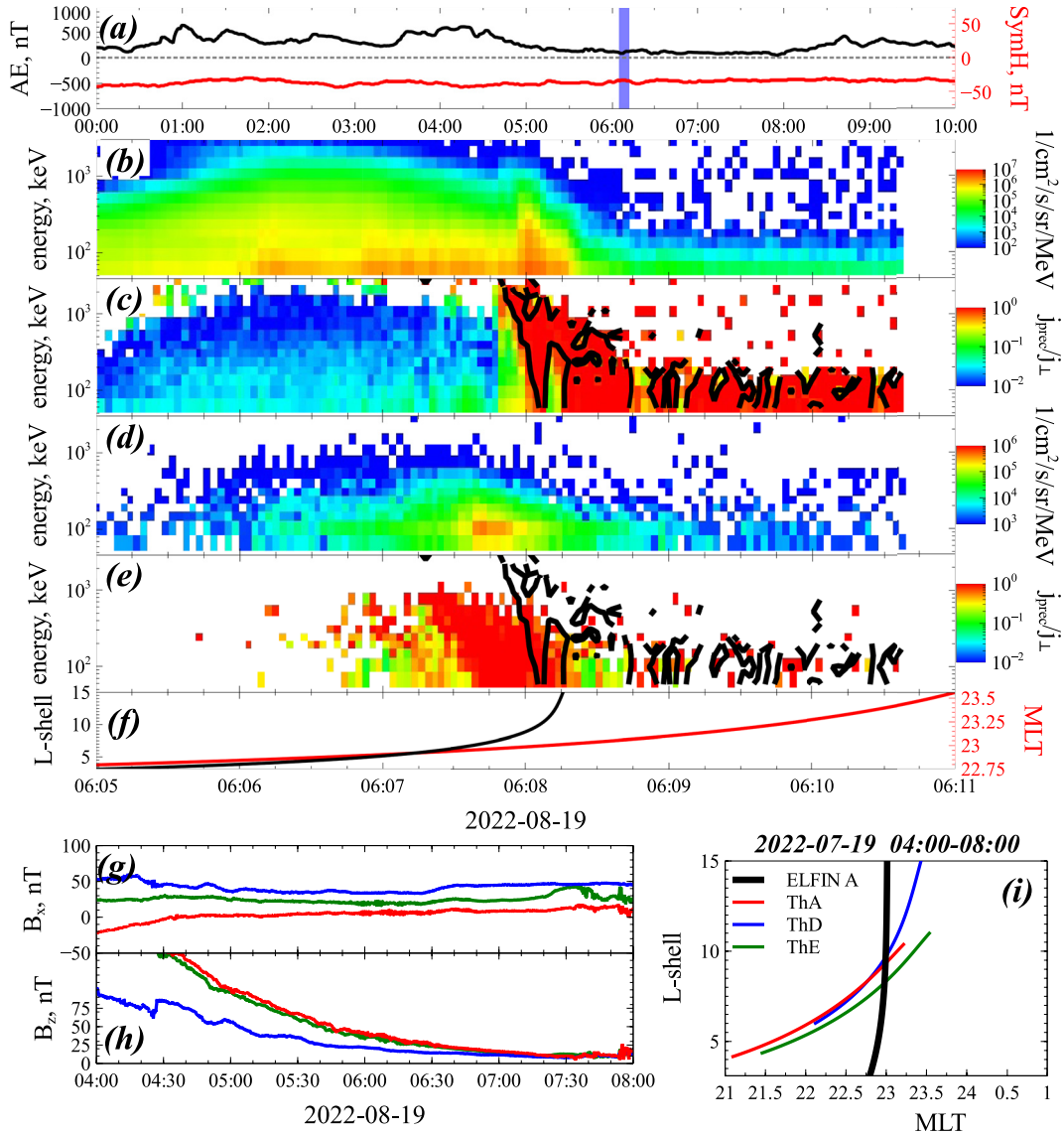

Figure 6. Overview of measurements during the event on 2022-08-19: (a) *AE* and *SymH* indices within a day. ELFIN orbit is denoted by a blue, vertical bar; (b, d) locally trapped electron and ion fluxes; (c, e) electron and ion precipitating-to-trapped flux ratio j_{prec}/j_{trap}, black contours in both panels mark where electron $j_{prec}/j_{trap} = 0.9$; (f) ELFIN *L*-shell and *MLT* from T89 (Tsyganenko, 1989) model; (g, h) B_x and B_z measurements from three THEMIS spacecraft during a three-hour interval; (i) ELFIN and THEMIS orbits projected to the (*MLT*, *L*) plane.

as seen in Panels (g, h)). Thus, the electron plasma sheet projection to the high latitudes shrinks and ELFIN measured only electron isotropy boundary around 21:58:40 UT. Well equatorward from this boundary, deep inside the outer radiation belt with trapped relativistic electron fluxes, ELFIN observes clear energy/*L* dispersed precipitation patterns over the 100 keV–3 MeV energy range. On the earthward side of this pattern, the energy of strongly precipitating electrons increases toward lower *L*-shells. This earthward side of the pattern nearly coincides with (or is even slightly equatorward from) the ion isotropy boundary of 2 MeV–50 keV ions, observed at 21:57:15–21:57:30 UT. Comparing the locations of this precipitation pattern and the trapped electron fluxes, we note that the equatorward boundary of precipitating electrons is also quite close to the plasmapause. Evidence of the plasmapause is seen in the trapped electron fluxes as a boundary between the outer radiation belt (with trapped fluxes decreasing as the energy increases) and the plasmasphere (with a gap in ~200–400 keV electron fluxes due to the very effective electron scattering by plasmapsheric hiss waves; see discussion of this feature of j_{trap} measured by ELFIN in Mourenas et al. (2021); Angelopoulos et al. (2022)).

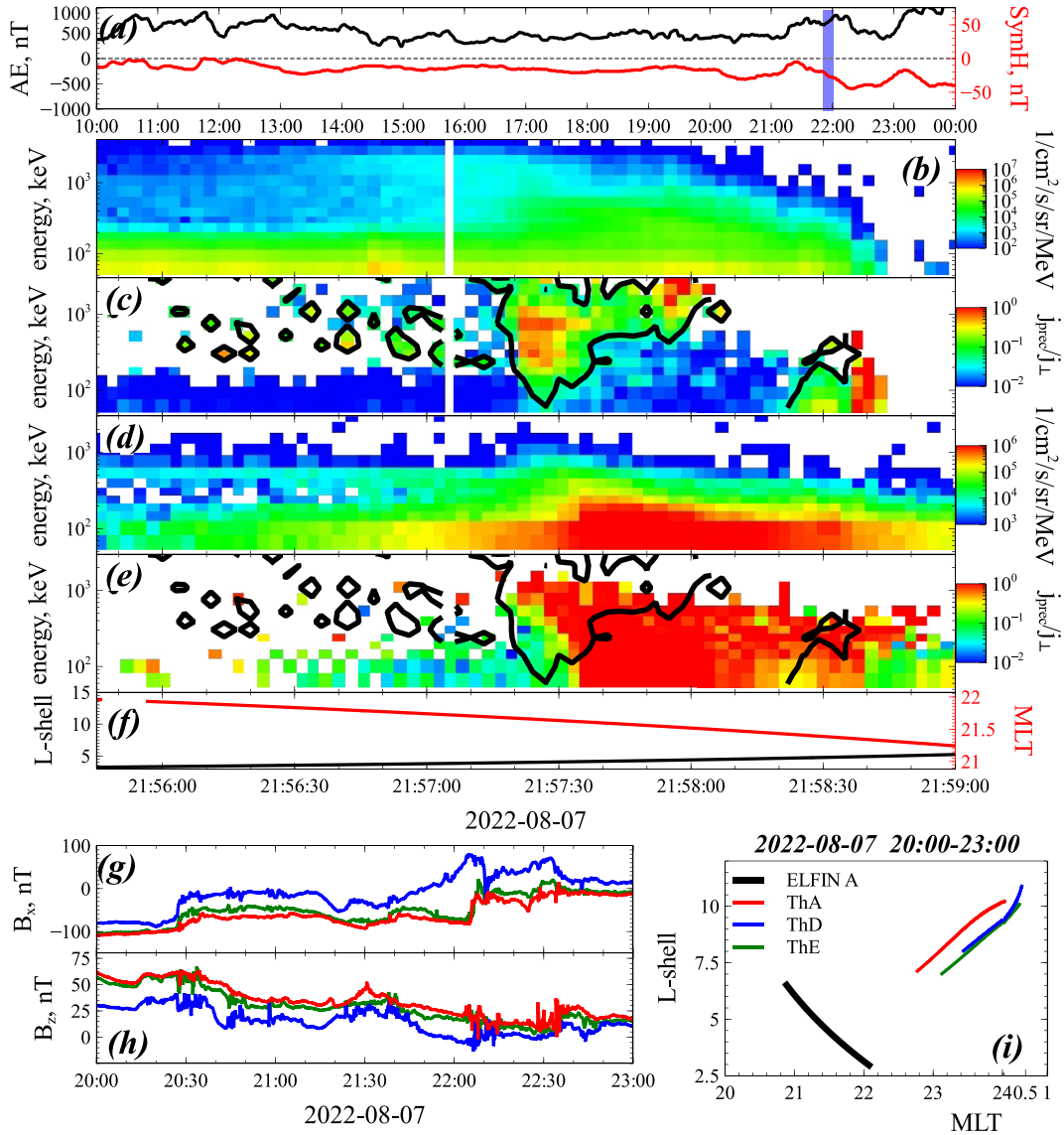

Figure 7. Overview of measurements during the event on 2022-08-07: (a) *AE* and *SymH* indices within a day, the ELFIN orbit is denoted by a blue, vertical bar; (b, d) locally trapped electron and ion fluxes; (c, e) electron and ion precipitating-to-trapped flux ratio j_{prec}/j_{trap}, black contours in both panels mark where electron $j_{prec}/j_{trap} = 0.9$; (f) ELFIN *L*-shell and *MLT* from T89 (Tsyganenko, 1989) model; (g, h) B_x and B_z measurements from three THEMIS spacecraft during a three-hour interval; (i) ELFIN and THEMIS orbits projected to the (*MLT*, *L*) plane.

4. Possible Mechanisms Responsible for Relativistic Electron Precipitation

Figures 3–6 show that dispersed electron precipitation patterns can be observed during different geomagnetic conditions equatorward from the electron isotropy boundary and around or poleward of the ion isotropy boundary, including within the ion plasma sheet. Several mechanisms can be responsible for such electron precipitation patterns. Before discussing those mechanisms, let us exclude one that is commonly responsible for electron losses in the outer radiation belt: electron scattering by whistler-mode waves. We note that the new dispersed electron precipitation patterns extend to the lowest observed energy, 50 keV, electrons (Figures 5 and 6). However, our observations show that the new dispersed precipitation can often occur only at high energies without concurrent intense precipitation at 50–100 keV. Since the efficiency of electron scattering by whistler-mode waves increases with decreasing energy (Albert, 2005; Glauert & Horne, 2005; Mourenas et al., 2012; Shprits et al., 2008), whistler-mode wave driven precipitation is always characterized by larger j_{prec}/j_{trap} at smaller energies; for example, at ELFIN, the electron precipitation driven by whistler-mode waves is characterized by a j_{prec}/j_{trap} peak at

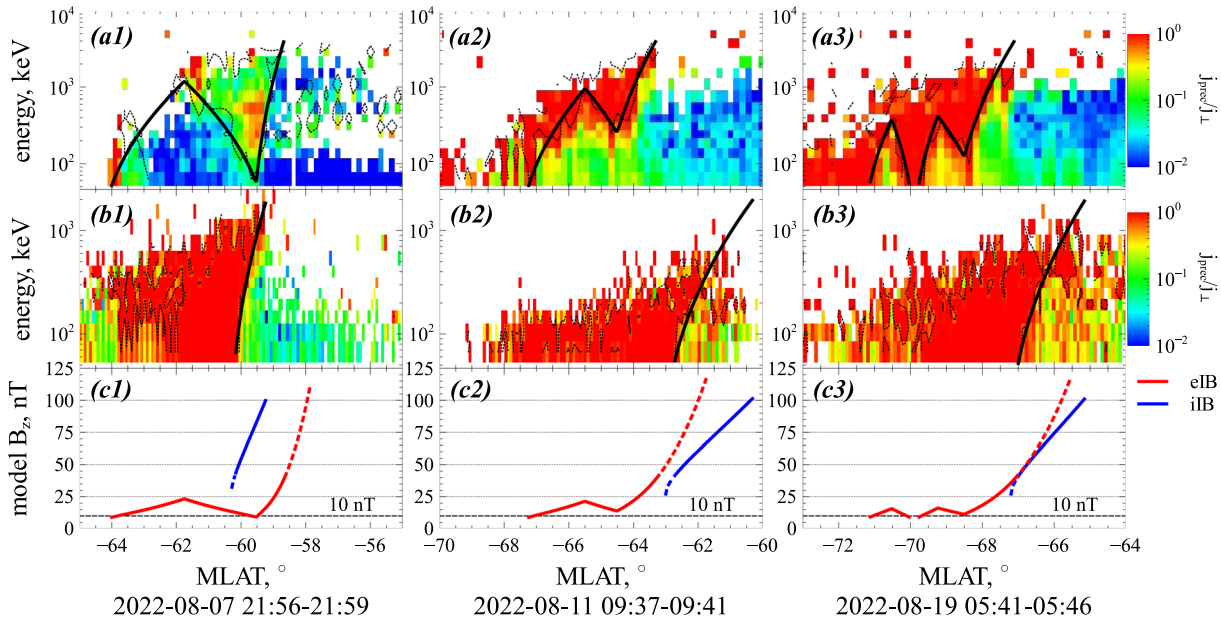

Figure 8. Panels (a, b) show electron and ion precipitating-to-trapped flux ratio for events from Figures 4, 5 and 7, shown in the left, middle and right columns, respectively. Black curves fit the boundary of the precipitation rate. Panels (c) show equatorial B_z (as a function of magnetic latitude) derived from equation $R_c/\rho = 8$ (Sergeev & Tsyganenko, 1982) with the current sheet $R_c = cB_z/4\pi j_{eq}$ and a constant equatorial current density j_{eq} = 10 nA/m^2. Solid red and blue lines show results for electrons and ions respectively; dashed lines are extrapolations.

50–100 keV (see examples of ELFIN observations in Tsai et al., 2022; Shi et al., 2022; Zhang et al., 2022). Thus, it is unlikely that whistler-mode wave scattering is the source of the observed precipitation throughout the entire period of the new dispersed electron precipitation pattern (i.e., it cannot be the sole reason for the precipitation across all energies, or the observed dispersion). Let us now discuss, below, three possible mechanisms for it.

4.1. Curvature Scattering

The clear energy versus *L*-shell dispersion of the strong precipitation ratio in this new precipitation pattern is reminiscent of a similar pattern due to curvature scattering, which forms the electron isotropy boundary at higher latitude. Curvature scattering deep inside the outer radiation belt would require significant deformation of the background magnetic field (Sergeev et al., 2023) used a magnetic field model (Tsyganenko, 1995) to investigate the possible magnetic field configuration in event #12 from Table 1, and showed that no reasonable magnetic field configuration can provide the observed electron precipitation equatorward from the isotropy boundary. To further verify this conclusion for events with ELFIN ion measurements, we examine precipitation patterns from Figures 4, 5, and 7. We perform a simplified estimate: we fit the boundary of the isotropic precipitation (both the classical isotropy boundary and the equatorward dispersed pattern) to a function that depends on latitude, so we have $E_{iso}(MLAT)$. Then we use the typical equation for conditions of curvature scattering, $R_c/\rho = 8$ (Sergeev & Tsyganenko, 1982), to determine the equatorial $B_z(MLAT)$ profile for a constant equatorial current density of 10 nA/m^2 (this is a large current density for the ring current ions, but still within the range of observations (see; C. Shen et al., 2014; Tan et al., 2022; Vallat et al., 2005; Yang et al., 2016) and model estimates (see Kubyshkina et al., 2009, 2011; Sergeev et al., 2023; Stephens et al., 2016)). The same $B_z(MLAT)$ profile is evaluated from the ion isotropy boundary. Figure 8 shows these $E_{iso}(MLAT)$ fittings and the derived $B_z(MLAT)$ from electron (red) and ion (blue) measurements. Note that the electron $B_z(MLAT)$ starts from ~10 nT in the plasma sheet latitudes, in agreement with THEMIS measurements in the near-Earth magnetotail.

For the event from Figure 7 (left column), the large difference between ion and electron $B_z(MLAT)$ profiles at each latitude, and the fact that (contrary to expectation from reasonable average models for the geomagnetic field) a stronger equatorial field is required at higher latitude to explain the ion dispersion compared to the weaker field required at a lower latitude for the electrons demonstrates that curvature scattering cannot be responsible for the dispersed electron precipitation pattern. For the events from 4, 5 (middle and right columns in Figure 8,

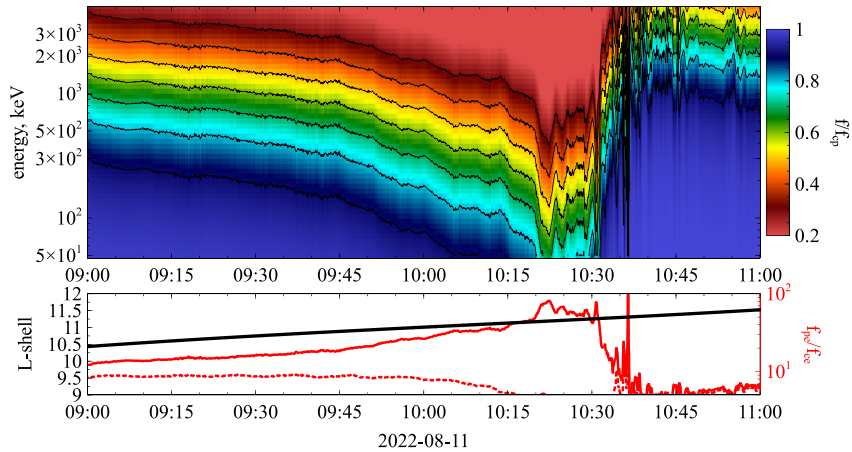

Figure 9. THEMIS E observations during a sub-interval from Figure 4. Bottom panel shows THEMIS *L*-shell and plasma frequency to electron gyrofrequency ratio at THEMIS location (dashed line) and with equatorial field B_z (solid line). Top panel shows the resonant electron energy as a function of EMIC wave frequency (normalized to the proton gyrofrequency); black traces mark contours of the resonant energy.

respectively), ion and electron $B_z(MLAT)$ profiles are in better agreement. Thus, for a strong, constant equatorial current density in the entire region of the outer radiation belt, the associated curvature scattering could explain the observed electron dispersed precipitation pattern. However, in addition to such a strong current density, one would need a non-monotonic mapping of $B_z(MLAT) \rightarrow B_z(L)$, one that attains local maxima and minima. Although such profiles have been suggested previously for the near-Earth magnetotail (Merkin et al., 2015; Sergeev et al., 2018; Sitnov et al., 2021), they have not been discussed in the context of the outer radiation belt (ring current region), where the equatorial magnetic field starts to be dominated by the Earth's dipole.

4.2. EMIC Waves

Resonance with EMIC waves is another candidate for relativistic electron scattering in the nightside injection region (see statistics of such nightside EMIC wave-driven precipitation events in Yahnin et al., 2016; Capannolo et al., 2022; Angelopoulos et al., 2022). However, in order for this mechanism to work, additional explanation should be provided to account for the scattering within the same precipitation structure of ~50 keV electrons (an energy much lower than the minimum resonance energy of EMIC waves, see Summers & Thorne, 2003; Kersten et al., 2014; Ni et al., 2015; Chen et al., 2019; Zhang et al., 2021) and about the energy versus *L*-shell dispersion. Nonresonant scattering (An et al., 2022; Chen et al., 2016) and hot plasma effects (e.g., Bashir et al., 2022; Chen et al., 2011; Silin et al., 2011) may decrease the energy of moderately scattered electrons to a few hundred keV, but can still not explain the observed strong scattering ($j_{prec}/j_{trap} \approx 1$) of electrons as low as 50 keV.

Interestingly, many of the dispersed precipitation patterns are observed during times of substorm growth phase, when the magnetotail current sheet thins and moves earthward, the equatorial magnetic field intensity decreases significantly, and the density of a cold plasma population significantly increases (Artemyev et al., 2016; Yushkov et al., 2021). Such a near-Earth magnetotail reconfiguration can create at the near-Earth equator a local magnetic field minimum, a plasma density maximum, and a localized strong earthward gradient in the plasma frequency to gyrofrequency ratio, f_{pe}/f_{ce}. The latter controls the EMIC wave minimum resonance energy (Summers & Thorne, 2003). Figure 9 shows a sub-interval of THEMIS E observations during the event from Figure 4, demonstrating this effect. The bottom panel shows the f_{pe}/f_{ce} ratio evaluated using the measured B_z magnetic field (assumed to equal the equatorial field) and the plasma density evaluated from the spacecraft potential (Bonnell et al., 2008; Nishimura et al., 2013). This ratio has a clear peak, as a function of time, interpreted as also a function of proximity to Earth (since the satellite was moving Earthward at that time, as seen in Panel (i) of Figure 4). We may use this peak to estimate the electron resonance energy with EMIC waves. This is demonstrated with the top panel of Figure 9. It shows the EMIC wave to ion cyclotron frequency ratio (black curves and color axis) as a function of minimum resonance energy (vertical axis) and time (horizontal axis). It demonstrates that for sufficiently high normalized wave frequency EMIC waves, $f/f_{cp} \sim 0.6$–0.8, the resonance energy can go

down to 50 keV due to the f_{pe}/f_{ce} increase. The reduction is interpreted to be both localized spatially and evolving temporally. The radial f_{pe}/f_{ce} gradient associated with the Earthward increase of the background magnetic field leads to an energy versus L-shell dispersion that would be similar to ELFIN observations. Although this mechanism of energy versus L-shell dispersed precipitation looks like a promising explanation, direct observations of EMIC waves in the outer radiation belt during the substorm growth phase (prior to hot ion injections) have not been previously reported. A slightly modified scenario that can explain the observations is the formation of a similar f_{pe}/f_{ce} gradient due to the development of a localized magnetic intensity depression from the diamagnetism of hot injected ions at a nearby magnetic sector just to the East of the observation location (Xia et al., 2019; H. Zhu et al., 2021; Yin et al., 2021). Such conditions (hot, drifting ions, low magnetic field intensity) are prone to EMIC wave excitation and the existence of sharp density gradients can result in a similarly sharp variation in electron resonance energy as a function of radial distance (He et al., 2017; Yin et al., 2022). Moreover, localized magnetic field depletion may enhance the curvature scattering from the same region of EMIC wave generation, which can thus combine these two mechanisms potentially responsible for the formation of dispersed relativistic electron precipitation patterns. However, this is yet to be verified by conjugate observations between equatorial and low-altitude spacecraft.

4.3. KAW Waves

The third mechanism possibly responsible for the observed dispersed electron precipitation signatures is electron scattering by kinetic Alfvén waves, which are often observed around the inner edge of the ion plasma sheet (e.g., E. V. Mishin, 2013; E. Mishin & Streltsov, 2022) and/or the plasma injection region (Malaspina et al., 2015). Such waves may resonate with electrons via drift-bounce resonance and can provide pitch-angle scattering with diffusion rate $D_{\alpha\alpha} \gtrsim 10^{-5}\cdot 1/\mathrm{s}$ (Chaston et al., 2018). Alternatively, Doppler shifted Landau resonance of energetic electrons and KAWs may provide $D_{\alpha\alpha} \gtrsim 10^{-4}\cdot 1/\mathrm{s}$ (Y. Shen et al., 2022). To estimate whether such a scattering rate is sufficiently large to explain the observed electron precipitation, we infer $D_{\alpha\alpha}$ from the observed j_{prec}/j_{trap}, using the equation from (Angelopoulos et al., 2022; Kennel & Petschek, 1966): $D_{\alpha\alpha} \approx 2\cdot(j_{prec}/j_{trap})^2\cdot\alpha_{LC}^2/\tau_b(\alpha_{LC})$, where α_{LC} is the equatorial loss-cone and τ_b is the electron bounce period. As shown in Figure 10, the dispersed electron precipitation patterns correspond to $D_{\alpha\alpha} > 10^{-4}/\mathrm{s}$. Note that there are significant uncertainties of the magnetic mapping of ELFIN to the equator, and thus values of α_{LC} and τ_b that depend on L-shell should be treated as rough estimates. Based on these estimates, the ELFIN-derived diffusion rate is comparable to the expected $D_{\alpha\alpha}$ due to KAWs (Chaston et al., 2018; Y. Shen et al., 2022). Therefore, KAWs generated by ion injections (around the inner edge of the ion current sheet) may be strong enough to explain the observed electron precipitation. However, this scenario requires additional refinement to account for the observed energy versus L-shell dispersion in the electron precipitation.

5. Discussion and Conclusions

In this study, we show a new type of relativistic electron precipitation deep inside the outer radiation belt, exhibiting clear dispersion pattern in the minimum energy of strong precipitating-to-trapped flux ratio (>0.5) versus L-shell (with higher energies at lower L-shells). This type of precipitation was observed around midnight during various moderate-to-high geomagnetic activity levels. These patterns demonstrate very strong precipitation at energies greater than the minimum energy of strong precipitation, having $j_{prec}/j_{trap} \sim 1$, and thus could contribute significantly to the rapid depletion of relativistic electron fluxes in the outer radiation belt. An interesting and important property of such strong precipitation patterns is their nightside location, whereas more traditional loss mechanisms are located predominantly on the day-side (magnetopause shadowing) and dusk flank (EMIC wave-driven precipitation).

We proposed three possible mechanisms for such precipitating patterns (curvature scattering, resonances with EMIC or KAW waves), but each of them alone cannot fully explain properties of the observed precipitation patterns:

- Curvature scattering may provide an explanation for those precipitation patterns observed closer to the classical electron isotropy boundary (far poleward from the ion isotropy boundary), but this would require quite strong equatorial current density within the outer radiation belt region.
- EMIC wave-driven precipitation may explain the observed precipitation in the presence of a strong, Earthward gradient of the plasma frequency to equatorial electron gyrofrequency ratio, for example, during the current

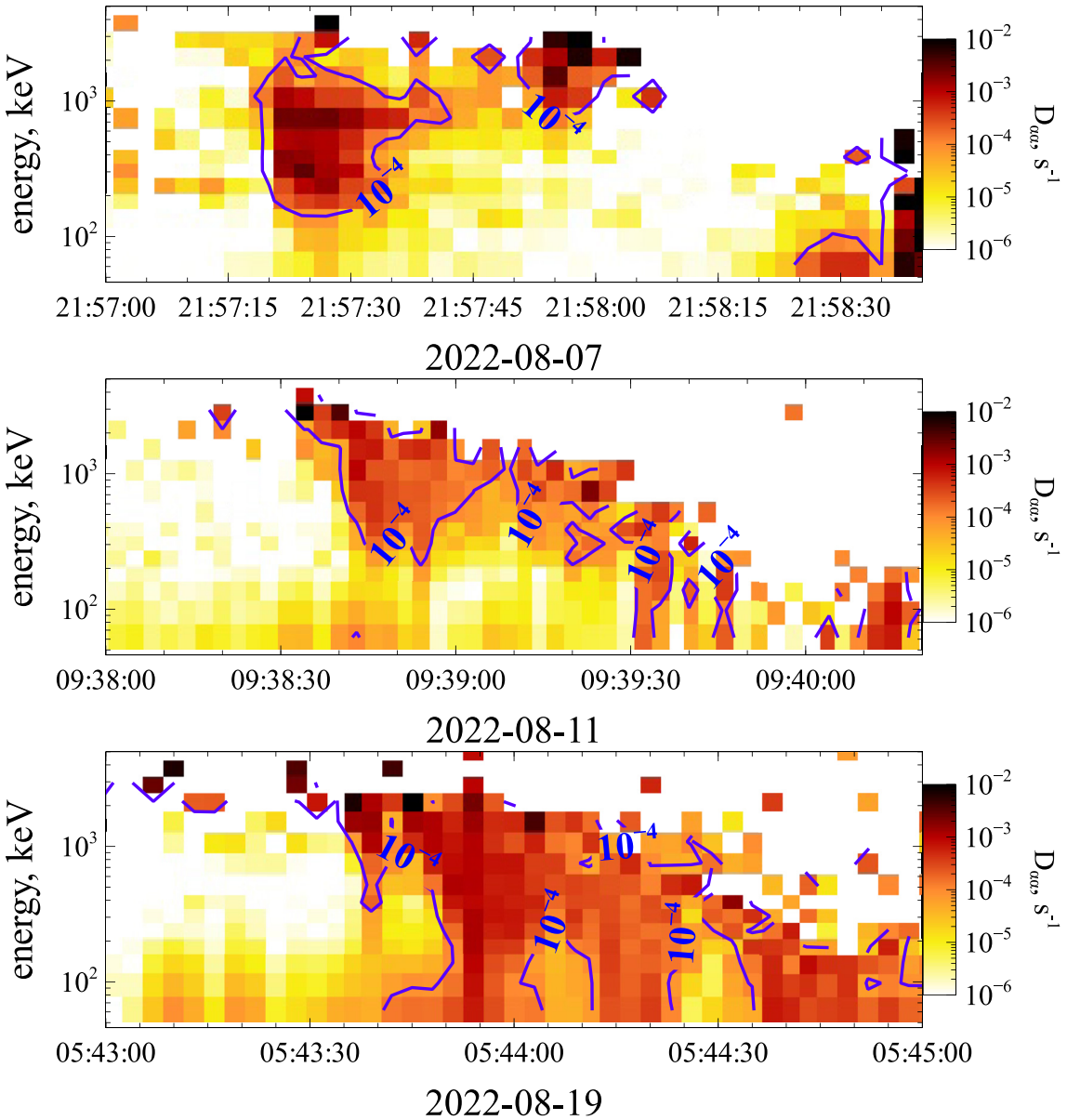

Figure 10. Estimated pitch-angle diffusion rates, $D_{\alpha\alpha} \approx 2 \cdot \left(j_{prec}/j_{trap}\right)^2 \alpha_{LC}^2/\tau_b$ (see details in Angelopoulos et al., 2022), for events from Figures 4, 5 and 7.

sheet thinning in the substorm growth phase; however, there has been no observational evidence of EMIC waves generated within the thinning current sheet.

- Energetic electron scattering by KAWs, which are often observed around ion injection region, inside outer radiation belt, may provide sufficiently strong scattering rates to explain the precipitation pattern; however, there is no good explanation on how KAW-driven scattering should provide an energy/*L*-shell dispersion of precipitating electrons.

Further investigations, including simulations and observations, are needed to reveal the specific mechanism(s) responsible for the energy versus *L*-shell dispersion in this new precipitation pattern.

Data Availability Statement

ELFIN data is available at ELFIN data is available at http://themis-data.igpp.ucla.edu/ela/, THEMIS data is available at http://themis.ssl.berkeley.edu. Data access and processing was done using SPEDAS V4.1, see Angelopoulos et al. (2019).

Acknowledgments
We acknowledge support by NASA awards 80NSSC23K0108, 80NSSC23K0403, 80NSSC20K0689, 80NSSC21K1320 and NNX14AN68G, NASA contract NAS5-02099, and NSF Grants 2021749, 1242918 and 2019914. We are grateful to NASA's CubeSat Launch Initiative for ELFIN's successful launch in the desired orbits. We acknowledge early support of ELFIN project by the AFOSR, under its University Nanosat Program, UNP-8 project, contract FA9453-12-D-0285, and by the California Space Grant program. We acknowledge the critical contributions of numerous volunteer ELFIN team student members.

References

Albert, J. M. (2005). Evaluation of quasi-linear diffusion coefficients for whistler mode waves in a plasma with arbitrary density ratio. *Journal of Geophysical Research*, *110*(A3), 3218. https://doi.org/10.1029/2004JA010844

An, X., Artemyev, A., Angelopoulos, V., Zhang, X., Mourenas, D., & Bortnik, J. (2022). Nonresonant scattering of relativistic electrons by electromagnetic ion cyclotron waves in Earth's radiation belts. *Physical Review Letters*, *129*(13), 135101. https://doi.org/10.1103/PhysRevLett.129.135101

Angelopoulos, V. (2008). The THEMIS mission. *Space Science Reviews*, *141*(1–4), 5–34. https://doi.org/10.1007/s11214-008-9336-1

Angelopoulos, V., Artemyev, A., Phan, T. D., & Miyashita, Y. (2020). Near-Earth magnetotail reconnection powers space storms. *Nature Physics*, *16*(3), 317–321. https://doi.org/10.1038/s41567-019-0749-4

Angelopoulos, V., Cruce, P., Drozdov, A., Grimes, E. W., Hatzigeorgiu, N., King, D. A., et al. (2019). The space physics environment data analysis system (SPEDAS). *Space Science Reviews*, *215*(1), 9. https://doi.org/10.1007/s11214-018-0576-4

Angelopoulos, V., Sibeck, D., Carlson, C. W., McFadden, J. P., Larson, D., Lin, R. P., et al. (2008). First results from the THEMIS mission. *Space Science Reviews*, *141*(1–4), 453–476. https://doi.org/10.1007/s11214-008-9378-4

Angelopoulos, V., Tsai, E., Bingley, L., Shaffer, C., Turner, D. L., Runov, A., et al. (2020). The ELFIN mission. *Space Science Reviews*, *216*(5), 103. https://doi.org/10.1007/s11214-020-00721-7

Angelopoulos, V., Zhang, X. J., Artemyev, A. V., Mourenas, D., Tsai, E., Wilkins, C., et al. (2022). Energetic electron precipitation driven by electromagnetic ion cyclotron waves from ELFIN's low altitude perspective. arXiv e-prints, arXiv:2211.15653. https://doi.org/10.48550/arXiv.2211.15653

Artemyev, A. V., Agapitov, O. V., Mozer, F. S., & Spence, H. (2015). Butterfly pitch angle distribution of relativistic electrons in the outer radiation belt: Evidence of nonadiabatic scattering. *Journal of Geophysical Research*, *120*(6), 4279–4297. https://doi.org/10.1002/2014JA020865

Artemyev, A. V., Angelopoulos, V., Runov, A., & Petrukovich, A. A. (2016). Properties of current sheet thinning at $x \sim 10$ to 12 R_E. *Journal of Geophysical Research*, *121*(7), 6718–6731. https://doi.org/10.1002/2016JA022779

Artemyev, A. V., Angelopoulos, V., Zhang, X. J., Runov, A., Petrukovich, A., Nakamura, R., et al. (2022). Thinning of the magnetotail current sheet inferred from low-altitude observations of energetic electrons. *Journal of Geophysical Research: Space Physics*, *127*(10), e2022JA030705. https://doi.org/10.1029/2022JA030705

Artemyev, A. V., Demekhov, A. G., Zhang, X. J., Angelopoulos, V., Mourenas, D., Fedorenko, Y. V., et al. (2021). Role of ducting in relativistic electron loss by whistler-mode wave scattering. *Journal of Geophysical Research: Space Physics*, *126*(11), e29851. https://doi.org/10.1029/2021JA029851

Artemyev, A. V., Orlova, K. G., Mourenas, D., Agapitov, O. V., & Krasnoselskikh, V. V. (2013). Electron pitch-angle diffusion: Resonant scattering by waves vs. nonadiabatic effects. *Annales Geophysicae*, *31*(9), 1485–1490. https://doi.org/10.5194/angeo-31-1485-2013

Auster, H. U., Glassmeier, K. H., Magnes, W., Aydogar, O., Baumjohann, W., Constantinescu, D., et al. (2008). The THEMIS fluxgate magnetometer. *Space Science Reviews*, *141*(1–4), 235–264. https://doi.org/10.1007/s11214-008-9365-9

Bashir, M. F., Artemyev, A., Zhang, X.-J., & Angelopoulos, V. (2022). Hot plasma effects on electron resonant scattering by electromagnetic ion cyclotron waves. *Geophysical Research Letters*, *49*(11), e99229. https://doi.org/10.1029/2022GL099229

Birmingham, T. J. (1984). Pitch angle diffusion in the Jovian magnetodisc. *Journal of Geophysical Research*, *89*(A5), 2699–2707. https://doi.org/10.1029/JA089iA05p02699

Blake, J. B., Mauk, B. H., Baker, D. N., Carranza, P., Clemmons, J. H., Craft, J., et al. (2016). The Fly's eye energetic particle spectrometer (FEEPS) sensors for the magnetospheric multiscale (MMS) Mission. *Space Science Reviews*, *199*(1–4), 309–329. https://doi.org/10.1007/s11214-015-0163-x

Bloch, T., Watt, C. E. J., Owens, M. J., Thompson, R. L., & Agiwal, O. (2021). Constraining the location of the outer boundary of Earth's outer radiation belt. *Earth and Space Science*, *8*(6), e01610. https://doi.org/10.1029/2020EA001610

Bonnell, J. W., Mozer, F. S., Delory, G. T., Hull, A. J., Ergun, R. E., Cully, C. M., et al. (2008). The electric field instrument (EFI) for THEMIS. *Space Science Reviews*, *141*(1–4), 303–341. https://doi.org/10.1007/s11214-008-9469-2

Burch, J. L., Moore, T. E., Torbert, R. B., & Giles, B. L. (2016). Magnetospheric multiscale overview and science objectives. *Space Science Reviews*, *199*(1–4), 5–21. https://doi.org/10.1007/s11214-015-0164-9

Capannolo, L., Li, W., Millan, R., Smith, D., Sivadas, N., Sample, J., & Shekhar, S. (2022). Relativistic electron precipitation near midnight: Drivers, distribution, and properties. *Journal of Geophysical Research: Space Physics*, *127*(1), e30111. https://doi.org/10.1029/2021JA030111

Chaston, C. C., Bonnell, J. W., Halford, A. J., Reeves, G. D., Baker, D. N., Kletzing, C. A., & Wygant, J. R. (2018). Pitch angle scattering and loss of radiation belt electrons in broadband electromagnetic waves. *Geophysical Research Letters*, *45*(18), 9344–9352. https://doi.org/10.1029/2018GL079527

Chen, L., Thorne, R. M., & Bortnik, J. (2011). The controlling effect of ion temperature on EMIC wave excitation and scattering. *Geophysical Research Letters*, *38*(16), L16109. https://doi.org/10.1029/2011GL048653

Chen, L., Thorne, R. M., Bortnik, J., & Zhang, X.-J. (2016). Nonresonant interactions of electromagnetic ion cyclotron waves with relativistic electrons. *Journal of Geophysical Research*, *121*(10), 9913–9925. https://doi.org/10.1002/2016JA022813

Chen, L., Thorne, R. M., & Horne, R. B. (2009). Simulation of EMIC wave excitation in a model magnetosphere including structured high-density plumes. *Journal of Geophysical Research*, *114*(A7), A07221. https://doi.org/10.1029/2009JA014204

Chen, L., Zhang, X.-J., Artemyev, A., Angelopoulos, V., Tsai, E., Wilkins, C., & Horne, R. B. (2022). Ducted chorus waves cause sub-relativistic and relativistic electron microbursts. *Geophysical Research Letters*, *49*(5), e97559. https://doi.org/10.1029/2021GL097559

Chen, L., Zhu, H., & Zhang, X. (2019). Wavenumber analysis of EMIC waves. *Geophysical Research Letters*, *46*(11), 5689–5697. https://doi.org/10.1029/2019GL082686

Chu, X., McPherron, R. L., Hsu, T.-S., Angelopoulos, V., Pu, Z., Yao, Z., et al. (2015). Magnetic mapping effects of substorm currents leading to auroral poleward expansion and equatorward retreat. *Journal of Geophysical Research: Space Physics*, *120*(1), 253–265. https://doi.org/10.1002/2014JA020596

Delcourt, D. C., Martin, R. F., Jr., & Alem, F. (1994). A simple model of magnetic moment scattering in a field reversal. *Geophysical Research Letters*, *21*(14), 1543–1546. https://doi.org/10.1029/94GL01291

Delcourt, D. C., Sauvaud, J. A., Martin, R. F., & Moore, T. E. (1995). Gyrophase effects in the centrifugal impulse model of particle motion in the magnetotail. *Journal of Geophysical Research*, *100*(A9), 17211–17220. https://doi.org/10.1029/95JA00657

Dubyagin, S., Apatenkov, S., Gordeev, E., Ganushkina, N., & Zheng, Y. (2021). Conditions of loss cone filling by scattering on the curved field lines for 30 keV protons during geomagnetic storm as inferred from numerical trajectory tracing. *Journal of Geophysical Research: Space Physics*, *126*(1), e28490. https://doi.org/10.1029/2020JA028490

Dubyagin, S., Sergeev, V. A., & Kubyshkina, M. V. (2002). On the remote sensing of plasma sheet from low-altitude spacecraft. *Journal of Atmospheric and Solar-Terrestrial Physics*, *64*(5–6), 567–572. https://doi.org/10.1016/S1364-6826(02)00014-7

Elliott, S. S., Breneman, A., Colpitts, C., Bortnik, J., Jaynes, A., Halford, A., et al. (2022). Understanding the properties, wave drivers, and impacts of electron microburst precipitation: Current understanding and critical knowledge gaps. *Frontiers in Astronomy and Space Sciences*, *9*, 1062422. https://doi.org/10.3389/fspas.2022.1062422

Glauert, S. A., & Horne, R. B. (2005). Calculation of pitch angle and energy diffusion coefficients with the PADIE code. *Journal of Geophysical Research*, *110*(A4), 4206. https://doi.org/10.1029/2004JA010851

Goldstein, J., Pascuale, S., & Kurth, W. S. (2019). Epoch-Based model for stormtime plasmapause location. *Journal of Geophysical Research: Space Physics*, *124*(6), 4462–4491. https://doi.org/10.1029/2018JA025996

Grach, V. S., Artemyev, A. V., Demekhov, A. G., Zhang, X.-J., Bortnik, J., Angelopoulos, V., et al. (2022). Relativistic electron precipitation by EMIC waves: Importance of nonlinear resonant effects. *Geophysical Research Letters*, *49*(17), e99994. https://doi.org/10.1029/2022GL099994

He, Z., Chen, L., Zhu, H., Xia, Z., Reeves, G. D., Xiong, Y., et al. (2017). Multiple-satellite observation of magnetic dip event during the substorm on 10 October 2013. *Geophysical Research Letters*, *44*(18), 9167–9175. https://doi.org/10.1002/2017GL074869

Imhof, W. L., Reagan, J. B., & Gaines, E. E. (1977). Fine-scale spatial structure in the pitch angle distributions of energetic particles near the midnight trapping boundary. *Journal of Geophysical Research*, *82*(32), 5215–5221. https://doi.org/10.1029/JA082i032p05215

Jun, C.-W., Miyoshi, Y., Kurita, S., Yue, C., Bortnik, J., Lyons, L., et al. (2021). The characteristics of EMIC waves in the magnetosphere based on the Van Allen Probes and Arase observations. *Journal of Geophysical Research: Space Physics*, *126*(6), e29001. https://doi.org/10.1029/2020JA029001

Jun, C. W., Yue, C., Bortnik, J., Lyons, L. R., Nishimura, Y., & Kletzing, C. (2019). EMIC wave properties associated with and without injections in the inner magnetosphere. *Journal of Geophysical Research: Space Physics*, *124*(3), 2029–2045. https://doi.org/10.1029/2018JA026279

Kennel, C. F., & Petschek, H. E. (1966). Limit on stably trapped particle fluxes. *Journal of Geophysical Research*, *71*, 1–28. https://doi.org/10.1029/jz071i001p00001

Kersten, T., Horne, R. B., Glauert, S. A., Meredith, N. P., Fraser, B. J., & Grew, R. S. (2014). Electron losses from the radiation belts caused by EMIC waves. *Journal of Geophysical Research*, *119*(11), 8820–8837. https://doi.org/10.1002/2014JA020366

Kubyshkina, M., Sergeev, V., Tsyganenko, N., Angelopoulos, V., Runov, A., Donovan, E., et al. (2011). Time-dependent magnetospheric configuration and breakup mapping during a substorm. *Journal of Geophysical Research*, *116*(A5), A00I27. https://doi.org/10.1029/2010JA015882

Kubyshkina, M., Sergeev, V., Tsyganenko, N., Angelopoulos, V., Runov, A., Singer, H., et al. (2009). Toward adapted time-dependent magnetospheric models: A simple approach based on tuning the standard model. *Journal of Geophysical Research*, *114*(A1), A00C21. https://doi.org/10.1029/2008JA013547

Li, W., Thorne, R. M., Bortnik, J., Nishimura, Y., Angelopoulos, V., Chen, L., et al. (2010). Global distributions of suprathermal electrons observed on THEMIS and potential mechanisms for access into the plasmasphere. *Journal of Geophysical Research*, *115*(A12), A00J10. https://doi.org/10.1029/2010JA015687

Malaspina, D. M., Claudepierre, S. G., Takahashi, K., Jaynes, A. N., Elkington, S. R., Ergun, R. E., et al. (2015). Kinetic Alfvén waves and particle response associated with a shock-induced, global ULF perturbation of the terrestrial magnetosphere. *Geophysical Research Letters*, *42*(21), 9203–9212. https://doi.org/10.1002/2015GL065935

Mauk, B. H., Blake, J. B., Baker, D. N., Clemmons, J. H., Reeves, G. D., Spence, H. E., et al. (2016). The energetic particle detector (EPD) investigation and the energetic ion spectrometer (EIS) for the magnetospheric multiscale (MMS) mission. *Space Science Reviews*, *199*(1–4), 471–514. https://doi.org/10.1007/s11214-014-0055-5

Merkin, V. G., Sitnov, M. I., & Lyon, J. G. (2015). Evolution of generalized two-dimensional magnetotail equilibria in ideal and resistive MHD. *Journal of Geophysical Research*, *120*(3), 1993–2014. https://doi.org/10.1002/2014JA020651

Millan, R. M., & Thorne, R. M. (2007). Review of radiation belt relativistic electron losses. *Journal of Atmospheric and Solar-Terrestrial Physics*, *69*(3), 362–377. https://doi.org/10.1016/j.jastp.2006.06.019

Mishin, E., & Streltsov, A. (2022). On the kinetic theory of subauroral arcs. *Journal of Geophysical Research: Space Physics*, *127*(8), e30667. https://doi.org/10.1029/2022JA030667

Mishin, E. V. (2013). Interaction of substorm injections with the subauroral geospace: 1. Multispacecraft observations of SAID. *Journal of Geophysical Research: Space Physics*, *118*(9), 5782–5796. https://doi.org/10.1002/jgra.50548

Miyoshi, Y., Saito, S., Kurita, S., Asamura, K., Hosokawa, K., Sakanoi, T., et al. (2020). Relativistic electron microbursts as high-energy tail of pulsating aurora electrons. *Geophysical Research Letters*, *47*(21), e90360. https://doi.org/10.1029/2020GL090360

Mourenas, D., Artemyev, A. V., Ripoll, J.-F., Agapitov, O. V., & Krasnoselskikh, V. V. (2012). Timescales for electron quasi-linear diffusion by parallel and oblique lower-band Chorus waves. *Journal of Geophysical Research*, *117*(A6), A06234. https://doi.org/10.1029/2012JA017717

Mourenas, D., Artemyev, A. V., Zhang, X. J., Angelopoulos, V., Tsai, E., & Wilkins, C. (2021). Electron lifetimes and diffusion rates inferred from ELFIN measurements at low altitude: First results. *Journal of Geophysical Research: Space Physics*, *126*(11), e29757. https://doi.org/10.1029/2021JA029757

Newell, P. T., Sergeev, V. A., Bikkuzina, G. R., & Wing, S. (1998). Characterizing the state of the magnetosphere: Testing the ion precipitation maxima latitude (b2i) and the ion isotropy boundary. *Journal of Geophysical Research*, *103*(A3), 4739–4746. https://doi.org/10.1029/97JA03622

Ni, B., Cao, X., Zou, Z., Zhou, C., Gu, X., Bortnik, J., et al. (2015). Resonant scattering of outer zone relativistic electrons by multiband EMIC waves and resultant electron loss time scales. *Journal of Geophysical Research*, *120*(9), 7357–7373. https://doi.org/10.1002/2015JA021466

Nikolaev, A. V., Sergeev, V. A., Tsyganenko, N. A., Kubyshkina, M. V., Opgenoorth, H., Singer, H., & Angelopoulos, V. (2015). A quantitative study of magnetospheric magnetic field line deformation by a two-loop substorm current wedge. *Annales Geophysicae*, *33*(4), 505–517. https://doi.org/10.5194/angeo-33-505-2015

Nishimura, Y., Bortnik, J., Li, W., Thorne, R. M., Ni, B., Lyons, L. R., et al. (2013). Structures of dayside whistler-mode waves deduced from conjugate diffuse aurora. *Journal of Geophysical Research: Space Physics*, *118*(2), 664–673. https://doi.org/10.1029/2012JA018242

O'Brien, T. P., & Moldwin, M. B. (2003). Empirical plasmapause models from magnetic indices. *Geophysical Research Letters*, *30*(4), 1152. https://doi.org/10.1029/2002GL016007

Runov, A., Sergeev, V. A., Nakamura, R., Baumjohann, W., Apatenkov, S., Asano, Y., et al. (2006). Local structure of the magnetotail current sheet: 2001 cluster observations. *Annales Geophysicae*, *24*(1), 247–262. https://doi.org/10.5194/angeo-24-247-2006

Russell, C. T., Anderson, B. J., Baumjohann, W., Bromund, K. R., Dearborn, D., Fischer, D., et al. (2016). The magnetospheric multiscale magnetometers. *Space Science Reviews*, *199*(1–4), 189–256. https://doi.org/10.1007/s11214-014-0057-3

Sergeev, V. A., Angelopoulos, V., Kubyshkina, M., Donovan, E., Zhou, X.-Z., Runov, A., et al. (2011). Substorm growth and expansion onset as observed with ideal ground-spacecraft THEMIS coverage. *Journal of Geophysical Research*, *116*(A5), A00I26. https://doi.org/10.1029/2010JA015689

Sergeev, V. A., Gordeev, E. I., Merkin, V. G., & Sitnov, M. I. (2018). Does a local B-minimum appear in the tail current sheet during a substorm growth phase? *Geophysical Research Letters*, *45*(6), 2566–2573. https://doi.org/10.1002/2018GL077183

Sergeev, V. A., Kubyshkina, M., Alexeev, I., Fazakerley, A., Owen, C., Baumjohann, W., et al. (2008). Study of near-Earth reconnection events with cluster and double star. *Journal of Geophysical Research*, *113*(A7), A07S36. https://doi.org/10.1029/2007JA012902

Sergeev, V. A., Kubyshkina, M. V., Semenov, V., Artemyev, A., Angelopoulos, V., & Runov, A. (2023). Unusual magnetospheric dynamics during intense substorm initiated by strong magnetospheric compression. *Journal of Geophysical Research: Space Physics*, *128*(11), e2023JA031536. https://doi.org/10.1029/2023JA031536

Sergeev, V. A., Malkov, M., & Mursula, K. (1993). Testing the isotropic boundary algorithm method to evaluate the magnetic field configuration in the tail. *Journal of Geophysical Research*, *98*(A5), 7609–7620. https://doi.org/10.1029/92JA02587

Sergeev, V. A., Nishimura, Y., Kubyshkina, M., Angelopoulos, V., Nakamura, R., & Singer, H. (2012). Magnetospheric location of the equatorward prebreakup arc. *Journal of Geophysical Research*, *117*(A1), A01212. https://doi.org/10.1029/2011JA017154

Sergeev, V. A., Sazhina, E. M., Tsyganenko, N. A., Lundblad, J. A., & Soraas, F. (1983). Pitch-angle scattering of energetic protons in the magnetotail current sheet as the dominant source of their isotropic precipitation into the nightside ionosphere. *Planetary Space Science*, *31*(10), 1147–1155. https://doi.org/10.1016/0032-0633(83)90103-4

Sergeev, V. A., & Tsyganenko, N. A. (1982). Energetic particle losses and trapping boundaries as deduced from calculations with a realistic magnetic field model. *Planatary Space Science*, *30*(10), 999–1006. https://doi.org/10.1016/0032-0633(82)90149-0

Shen, C., Yang, Y. Y., Rong, Z. J., Li, X., Dunlop, M., Carr, C. M., et al. (2014). Direct calculation of the ring current distribution and magnetic structure seen by Cluster during geomagnetic storms. *Journal of Geophysical Research*, *119*(4), 2458–2465. https://doi.org/10.1002/2013JA019460

Shen, Y., Artemyev, A., Runov, A., Angelopoulos, V., Liu, J., Zhang, X.-J., et al. (2023). Energetic electron flux dropouts measured by elfin in the ionospheric projection of the plasma sheet. *Journal of Geophysical Research: Space Physics*, *128*(9), e2023JA031631. https://doi.org/10.1029/2023JA031631

Shen, Y., Artemyev, A., Vasko, I., Zhang, X.-J., Angelopoulos, V., An, X., & Runov, A. (2022). Energetic electron scattering by kinetic Alfvén waves at strong magnetic field gradients of dipolarization front. *Physics of Plasmas*, *29*(8), 082901. https://doi.org/10.1063/5.0096338

Shi, X., Zhang, X.-J., Artemyev, A., Angelopoulos, V., Hartinger, M. D., Tsai, E., & Wilkins, C. (2022). On the role of ULF waves in the spatial and temporal periodicity of energetic electron precipitation. *Journal of Geophysical Research: Space Physics*, *127*(12), e2022JA030932. https://doi.org/10.1029/2022JA030932

Shprits, Y. Y., Subbotin, D. A., Meredith, N. P., & Elkington, S. R. (2008). Review of modeling of losses and sources of relativistic electrons in the outer radiation belt II: Local acceleration and loss. *Journal of Atmospheric and Solar-Terrestrial Physics*, *70*(14), 1694–1713. https://doi.org/10.1016/j.jastp.2008.06.014

Silin, I., Mann, I. R., Sydora, R. D., Summers, D., & Mace, R. L. (2011). Warm plasma effects on electromagnetic ion cyclotron wave MeV electron interactions in the magnetosphere. *Journal of Geophysical Research*, *116*(A5), A05215. https://doi.org/10.1029/2010JA016398

Sitnov, M. I., Stephens, G., Motoba, T., & Swisdak, M. (2021). Data mining reconstruction of magnetotail reconnection and implications for its first-principle modeling. *Frontiers in Physics*, *9*, 90. https://doi.org/10.3389/fphy.2021.644884

Sivadas, N., Semeter, J., Nishimura, Y., & Mrak, S. (2019). Optical signatures of the outer radiation belt boundary. *Geophysical Research Letters*, *46*(15), 8588–8596. https://doi.org/10.1029/2019GL083908

Stephens, G. K., Sitnov, M. I., Ukhorskiy, A. Y., Roelof, E. C., Tsyganenko, N. A., & Le, G. (2016). Empirical modeling of the storm time innermost magnetosphere using Van Allen Probes and THEMIS data: Eastward and banana currents. *Journal of Geophysical Research*, *121*(1), 157–170. https://doi.org/10.1002/2015JA021700

Summers, D., & Thorne, R. M. (2003). Relativistic electron pitch-angle scattering by electromagnetic ion cyclotron waves during geomagnetic storms. *Journal of Geophysical Research*, *108*(A4), 1143. https://doi.org/10.1029/2002JA009489

Tan, X., Dunlop, M. W., Dong, X. C., Yang, Y. Y., Du, Y. S., Shen, C., et al. (2022). Ring current morphology from mms observations. *Journal of Geophysical Research: Space Physics*, *128*(4), e2023JA031372. https://doi.org/10.1029/2023JA031372

Thorne, R. M., & Kennel, C. F. (1971). Relativistic electron precipitation during magnetic storm main phase. *Journal of Geophysical Research*, *76*(19), 4446–4453. https://doi.org/10.1029/JA076i019p04446

Thorne, R. M., O'Brien, T. P., Shprits, Y. Y., Summers, D., & Horne, R. B. (2005). Timescale for MeV electron microburst loss during geomagnetic storms. *Journal of Geophysical Research*, *110*(A9), 9202. https://doi.org/10.1029/2004JA010882

Tsai, E., Artemyev, A., Zhang, X.-J., & Angelopoulos, V. (2022). Relativistic electron precipitation driven by nonlinear resonance with whistler-mode waves. *Journal of Geophysical Research: Space Physics*, *127*(5), e30338. https://doi.org/10.1029/2022JA030338

Tsyganenko, N. A. (1989). A magnetospheric magnetic field model with a warped tail current sheet. *Planatary Space Science*, *37*(1), 5–20. https://doi.org/10.1016/0032-0633(89)90066-4

Tsyganenko, N. A. (1995). Modeling the Earth's magnetospheric magnetic field confined within a realistic magnetopause. *Journal of Geophysical Research*, *100*(A4), 5599–5612. https://doi.org/10.1029/94JA03193

Vallat, C., Dandouras, I., Dunlop, M., Balogh, A., Lucek, E., Parks, G. K., et al. (2005). First current density measurements in the ring current region using simultaneous multi-spacecraft CLUSTER-FGM data. *Annales Geophysicae*, *23*(5), 1849–1865. https://doi.org/10.5194/angeo-23-1849-2005

Walsh, B. M., Hull, A. J., Agapitov, O., Mozer, F. S., & Li, H. (2020). A census of magnetospheric electrons from several ev to 30 kev. *Journal of Geophysical Research: Space Physics*, *125*(5), e2019JA027577. https://doi.org/10.1029/2019JA027577

Wilkins, C., Angelopoulos, V., Runov, A., Artemyev, A., Zhang, X.-J., Liu, J., & Tsai, E. (2023). Statistical characteristics of the electron isotropy boundary. arXiv e-prints, arXiv:2305.16260. https://doi.org/10.48550/arXiv.2305.16260

Xia, Z., Chen, L., Artemyev, A., Zhu, H., Jordanova, V. K., & Zheng, L. (2019). The effects of localized thermal pressure on equilibrium magnetic fields and particle drifts in the inner magnetosphere. *Journal of Geophysical Research: Space Physics*, *124*(7), 5129–5142. https://doi.org/10.1029/2018JA026043

Yahnin, A. G., Sergeev, V. A., Gvozdevsky, B. B., & Vennerstrøm, S. (1997). Magnetospheric source region of discrete auroras inferred from their relationship with isotropy boundaries of energetic particles. *Annales Geophysicae*, *15*(8), 943–958. https://doi.org/10.1007/s00585-997-0943-z

Yahnin, A. G., Yahnina, T. A., Semenova, N. V., Gvozdevsky, B. B., & Pashin, A. B. (2016). Relativistic electron precipitation as seen by NOAA POES. *Journal of Geophysical Research: Space Physics*, *121*(9), 8286–8299. https://doi.org/10.1002/2016JA022765

Yang, Y. Y., Shen, C., Dunlop, M., Rong, Z. J., Li, X., Angelopoulos, V., et al. (2016). Storm time current distribution in the inner equatorial magnetosphere: THEMIS observations. *Journal of Geophysical Research*, *121*(6), 5250–5259. https://doi.org/10.1002/2015JA022145

Yin, Z.-F., Zhou, X.-Z., Hu, Z.-J., Yue, C., Zong, Q.-G., Hao, Y.-X., et al. (2022). Localized excitation of electromagnetic ion cyclotron waves from anisotropic protons filtered by magnetic dips. *Journal of Geophysical Research: Space Physics*, *127*(6), e30531. https://doi.org/10.1029/2022JA030531

Yin, Z.-F., Zhou, X.-Z., Zong, Q.-G., Liu, Z.-Y., Yue, C., Xiong, Y., et al. (2021). Inner magnetospheric magnetic dips and energetic protons trapped therein: Multi spacecraft observations and simulations. *Geophysical Research Letters*, *48*(7), e92567. https://doi.org/10.1029/2021GL092567

Yushkov, E., Petrukovich, A., Artemyev, A., & Nakamura, R. (2021). Thermodynamics of the magnetotail current sheet thinning. *Journal of Geophysical Research: Space Physics*, *126*(4), e2020JA028969. https://doi.org/10.1029/2020JA028969

Zhang, X.-J., Angelopoulos, V., Mourenas, D., Artemyev, A., Tsai, E., & Wilkins, C. (2022). Characteristics of electron microburst precipitation based on high-resolution ELFIN measurements. *Journal of Geophysical Research: Space Physics*, *127*(5), e30509. https://doi.org/10.1029/2022JA030509

Zhang, X. J., Mourenas, D., Shen, X. C., Qin, M., Artemyev, A. V., Ma, Q., et al. (2021). Dependence of relativistic electron precipitation in the ionosphere on EMIC wave minimum resonant energy at the conjugate equator. *Journal of Geophysical Research: Space Physics*, *126*(5), e29193. https://doi.org/10.1029/2021JA029193

Zhu, H., Chen, L., Artemyev, A. V., Zhang, X.-J., & Breneman, A. W. (2021). Superposed epoch analyses of electron-driven and proton-driven magnetic dips. *Geophysical Research Letters*, *48*(21), e94934. https://doi.org/10.1029/2021GL094934

Zhu, M., Yu, Y., Tian, X., Shreedevi, P. R., & Jordanova, V. K. (2021). On the ion precipitation due to field line curvature (FLC) and EMIC wave scattering and their subsequent impact on ionospheric electrodynamics. *Journal of Geophysical Research: Space Physics*, *126*(3), e28812. https://doi.org/10.1029/2020JA028812